Icarus 212 (2011) 762–778

Contents lists available at ScienceDirect

Icarus

journal homepage: www.elsevier.com/locate/icarus

Titan's aerosol and stratospheric ice opacities between 18 and 500 μm: Vertical and spectral characteristics from Cassini CIRS

Carrie M. Anderson [a,*], Robert E. Samuelson [b]

[a] NASA GSFC, Solar System Exploration Division, Greenbelt, MD 20771, United States
[b] University of Maryland, Department of Astronomy, College Park, MD 20742, United States

ARTICLE INFO

Article history:
Received 16 September 2010
Revised 25 January 2011
Accepted 26 January 2011
Available online 1 February 2011

Keywords:
Titan
Radiative transfer
Ices

ABSTRACT

Vertical distributions and spectral characteristics of Titan's photochemical aerosol and stratospheric ices are determined between 20 and 560 cm^{-1} (500–18 μm) from the Cassini Composite Infrared Spectrometer (CIRS). Results are obtained for latitudes of 15°N, 15°S, and 58°S, where accurate temperature profiles can be independently determined.

In addition, estimates of aerosol and ice abundances at 62°N relative to those at 15°S are derived. Aerosol abundances are comparable at the two latitudes, but stratospheric ices are ~3 times more abundant at 62°N than at 15°S. Generally, nitrile ice clouds (probably HCN and HC_3N), as inferred from a composite emission feature at ~160 cm^{-1}, appear to be located over a narrow altitude range in the stratosphere centered at ~90 km. Although most abundant at high northern latitudes, these nitrile ice clouds extend down through low latitudes and into mid southern latitudes, at least as far as 58°S.

There is some evidence of a second ice cloud layer at ~60 km altitude at 58°S associated with an emission feature at ~80 cm^{-1}. We speculate that the identify of this cloud may be due to C_2H_6 ice, which in the vapor phase is the most abundant hydrocarbon (next to CH_4) in the stratosphere of Titan.

Unlike the highly restricted range of altitudes (50–100 km) associated with organic condensate clouds, Titan's photochemical aerosol appears to be well-mixed from the surface to the top of the stratosphere near an altitude of 300 km, and the spectral shape does not appear to change between 15°N and 58°S latitude. The ratio of aerosol-to-gas scale heights range from 1.3–2.4 at about 160 km to 1.1–1.4 at 300 km, although there is considerable variability with latitude. The aerosol exhibits a very broad emission feature peaking at ~140 cm^{-1}. Due to its extreme breadth and low wavenumber, we speculate that this feature may be caused by low-energy vibrations of two-dimensional lattice structures of large molecules. Examples of such molecules include polycyclic aromatic hydrocarbons (PAHs) and nitrogenated aromatics.

Finally, volume extinction coefficients $N\chi_E$ derived from 15°S CIRS data at a wavelength of $\lambda = 62.5$ μm are compared with those derived from the 10°S Huygens Descent Imager/Spectral Radiometer (DISR) data at 1.583 μm. This comparison yields volume extinction coefficient ratios $N\chi_E(1.583\ \mu m)/N\chi_E(62.5\ \mu m)$ of roughly 70 and 20, respectively, for Titan's aerosol and stratospheric ices. The inferred particle cross-section ratios $\chi_E(1.583\ \mu m)/\chi_E(62.5\ \mu m)$ appear to be consistent with sub-micron size aerosol particles, and effective radii of only a few microns for stratospheric ice cloud particles.

Published by Elsevier Inc.

1. Introduction

Titan's ubiquitous aerosol is the end result of complex hydrocarbon-nitrile photochemistry occurring at altitudes as high as ~1100 km (Waite et al., 2005, 2007). It plays a vital role in the radiative heating and cooling of the atmosphere. Aerosol heating on Titan is dominantly responsible for the largest stratospheric thermal inversion of any object in the solar system (Samuelson, 1983; McKay et al., 1989; Hanel et al., 2003), and aerosol shielding of Titan's surface from solar irradiation is responsible for inhibiting turbulent convection in the troposphere (McKay et al., 1991). The tropospheric temperature profile becomes subadiabatic, except possibly for the lowest 2–3 km, even in the presence of greenhouse warming from collision-induced absorption (CIA) from various pair combinations of H_2, N_2, and CH_4. This lack of turbulent convection frictionally decouples the atmosphere from the surface, enabling dynamical spin-up of Titan's initially slowly rotating atmosphere, leading to high superrotating zonal (east–west) wind velocities in Titan's stratosphere (Del Genio et al., 1993). These high wind velocities are variable with altitude, and the resulting dynamical shear quickly leads to a uniform global coverage of aerosol on Titan.

* Corresponding author. Fax: +1 301 286 1683.
E-mail address: carrie.m.anderson@nasa.gov (C.M. Anderson).

0019-1035/$ - see front matter Published by Elsevier Inc.
doi:10.1016/j.icarus.2011.01.024

Our knowledge of Titan's aerosol has gradually developed over the past 30 years, based on analyses of data obtained from various instruments found on Voyager, the Hubble Space Telescope, ground-based facilities, the Huygens Probe, and Cassini. Titan's optically thick stratospheric aerosol obscures the lower atmosphere and surface at visible wavelengths (Smith et al., 1981, 1982; Rages et al., 1983) and becomes increasingly transparent with longer wavelengths (McKay et al., 1989, 2001; Courtin et al., 1991; Karkoschka and Erich, 1994, 1998; Coustenis et al., 1995; Lorenz et al., 2001, 2004), allowing thermal infrared radiation to escape to space. Laboratory-created aerosols, termed *tholin* (Khare et al., 1984), match Titan's geometric albedo spectrum across UV to near-IR wavelengths, with better results assuming fractal aggregates instead of spherical particles (McKay et al., 1989, 2001; Toon et al., 1992; Rannou et al., 1995; see McKay et al. (2001), for a detailed review of Titan's aerosols through 2001). Although Titan's aerosol was initially thought to form via neutral CH_4 and N_2 chemistry around an altitude of 400 km (McKay et al., 1989; Toon et al., 1992; Rannou et al., 1995; McKay et al., 2001), recent observations obtained from the Cassini Ion and Neutral Mass Spectrometer (INMS) and the Ion Beam Spectrometer (IBS) suggest that the aerosol begins to form near 1100 km. At this altitude, large molecules with masses as high as ~350 dalton are detectable and are suspected to be important components in the formation of Titan's aerosol from complex neutral and ion chemistry (Young et al., 2004; Waite et al., 2005, 2007).

In situ measurements recorded by the Descent Imager/Spectral Radiometer (DISR) onboard the Huygens probe constrain the altitude and spectral dependence of the aerosol optical properties and the vertical distribution of the aerosol opacity between 0.35 μm and 1.6 μm at 10°S. Tomasko et al. (2008) find the aerosol single scattering albedo to be uniform with height above 140 km and below 80 km, and to increase linearly between 80 and 140 km, possibly due to condensation of organics. They determine the aerosol number density at 80 km to be roughly 5 cm^{-3}, decreasing to higher altitudes with a 65 km scale height. The aerosol opacity varies as $\lambda^{-2.34}$ above 80 km, $\lambda^{-1.41}$ between 80 and 30 km, and $\lambda^{-0.97}$ below 30 km. The small aerosol opacity below 30 km is indicative of aerosol growth, perhaps due to the incorporation of methane ice into aerosol particles. We refer the reader to Tomasko et al. (2008) for a detailed explanation of the DISR measurements and results, and to Tomasko and West (2009) for a thorough review of Titan's aerosols.

Aerosol optical cross-sections are much smaller in the thermal infrared than at shorter wavelengths. For limb observations, optical path lengths of unity tend to occur at mesospheric altitudes for reflected solar wavelengths and at stratospheric altitudes for thermal infrared wavelengths. For example, Rages and Pollack (1983) found it difficult to infer aerosol vertical distributions below 250 km with Voyager limb observations at visible wavelengths. On the other hand, limb observations in the thermal infrared can easily reach the tropopause and below, depending on the wavenumber. Samuelson and Mayo (1991) conducted the first analysis of the vertical distribution of aerosol between the tropopause (~40 km) and upper stratosphere (~300 km) from Voyager Infrared Interferometer Spectrometer (IRIS) far-IR limb observations. They utilized limb spectra between 69°N and 78°N and found the stratospheric opacities to monotonically increase with increasing wavenumber between 250 and 600 cm^{-1}. This trend becomes more drastic with decreasing altitude, suggesting that the aerosol is responsible for the opacity at higher altitudes and condensed organics are responsible for the opacity lower down in the stratosphere, at least at high northern latitudes.

In this present work, we utilize Composite Infrared Spectrometer (CIRS) focal plane 1 (FP1) FIR limb spectra of Titan at latitudes 15°N, 15°S, and 58°S to infer the vertical variations of Titan's stratospheric ice abundances, as well as those of the aerosol from the surface to an altitude of 300 km. Spectral variations of each component are obtained across the spectral range $20 \leqslant \nu \leqslant 560\ cm^{-1}$. The physical principles behind our approach are explained in Section 2, followed by a description of the observations and CIRS instrument in Section 3. In Section 4, we discuss the important opacity sources contained in Titan's atmosphere, and in Section 5 we describe our temperature structure retrieval method. Section 6 details the implementation of our radiative transfer model, and results are shown in Section 7. Implications of the results are discussed in Section 8. Included in this section is a detailed discussion of a comparison of our results with those of de Kok et al. (2007), who investigated the same spectral region. Finally, our main conclusions are summarized in Section 9.

2. Physical basis

Our ultimate interest is to identify and map out the abundances, vertical distributions, and spectral characteristics of the particulate matter in Titan's atmosphere as functions of latitude, using data primarily from the Cassini CIRS instrument. This requires deriving aerosol and stratospheric cloud properties from solutions to the radiative transfer equation for realistic model atmospheres.

We assume spherical shell geometry. In the absence of scattering, the transfer equation can be written

$$I(0,\mu_0) = I(\tau_1,\mu_1)exp\left(-\int_0^{\tau_1}\frac{d\tau}{\mu}\right) + \int_0^{\tau_1} B(\tau)e^{\frac{-\tau}{\mu}}\frac{d\tau}{\mu}, \quad (1)$$

where $I(\tau_1,\mu_1)$ is the surface intensity in the direction $\mu = \mu_1$ at an optical depth $\tau = \tau_1$, and $I(0,\mu_0)$ is the intensity of radiation at the top of the atmosphere (optical depth $\tau = 0$) in the direction μ_0; the direction cosine μ is variable with τ. If the path length of radiation is along a tangent ray through the atmosphere that does not intersect the surface, the surface intensity must be replaced by an integral along the line-of-sight through the "back half" of the emitting atmosphere,

$$I(\tau_1,\mu_1) = \int_0^{\tau_1} B(\tau)exp\left[-\frac{(\tau_1-\tau)}{|\mu|}\right]\frac{d\tau}{|\mu|}, \quad (2)$$

where τ_1 is now the normal optical depth at the point of tangency.

Uniqueness of solution requires physical constraints. We choose to smooth the functional dependences that relate various physical parameters so that noise in the system will not cause the solutions to be unstable. Our procedure is to construct logically arbitrary but physically reasonable analytic expressions containing these parameters. We then adjust the parameters by fitting radiative transfer solutions of models defined by the analytic expressions. We adopt the *Levenberg–Marquardt* nonlinear least-squares technique (see *e.g.* Marquardt, 1963) for fitting these models to the data. Uniqueness is achieved by minimizing the chi-squared merit function,

$$\chi^2 = \sum_{i=1}^{n}\left(\frac{I_{i,obs} - I_{i,mod}}{\sigma_i}\right)^2, \quad (3)$$

where i is the independent variable, σ_i is the standard deviation, and $I_{i,obs}$ and $I_{i,mod}$ are respectively the observed and model spectral intensities.

Scans across the limb that are perpendicular to it are the best way to infer vertical distributions. In this case the independent variable i in Eq. (3) is the tangent height h above (+) or below (−) the solid surface limb of Titan. We plot intensity vs. tangent height from the data at each wavenumber and then fit a parameterized model to it. Each particulate component has a unique chemistry; therefore, its spectral characteristics must be independent of altitude.

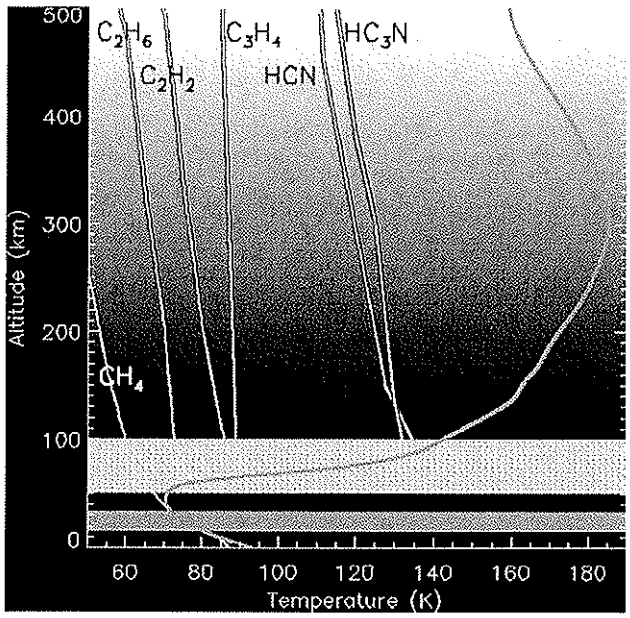

Fig. 1. Anticipated vertical distributions of particulates in Titan's atmosphere. Variable density of the photochemical aerosol is illustrated by white and pale yellow at the top (low density) to dark brown at the bottom (high density). Superimposed are the temperature profile at 15°S (blue curve) and several nitrile and hydrocarbon saturation vapor pressure curves. Condensation is possible where the saturation vapor pressure curves intersect the temperature profile, indicated by the pale, stippled band between 50 and 100 km. The single exception is CH_4, for which condensation is limited to the upper troposphere, as indicated by the thinner orange band.

Fig. 1 illustrates the general vertical distribution characteristics anticipated for Titan's particulates. We expect a photochemical aerosol to be mixed throughout the atmosphere, possibly with a somewhat greater scale height than the pressure scale height above an altitude of 80 km or so (Samuelson and Mayo, 1991; de Kok et al., 2007; Vinatier et al., 2010). Below 80 km, there is evidence, at least at low latitudes, that the aerosol volume extinction coefficient (and hence abundance) may be roughly constant with altitude (see Tomasko et al., 2008).

We therefore assume that the vertical distribution of the aerosol can be approximated by piecing together exponential variations in abundance with altitude over moderate altitude ranges above 80 km. Thus

$$N\chi_{iv} = N\chi_{0iv} e^{-c_i(z_i - z_{0i})} \tag{4}$$

over a limited altitude range, denoted by the subscript i, where $N\chi_{iv}$ is the volume absorption coefficient at wavenumber v, z_i is altitude, and $N\chi_{0iv}$ is the value of $N\chi_{iv}$ at a reference altitude z_{0i}. The unknown parameters c_i are to be evaluated by least-squares fitting to limb scan data at each wavenumber; the c_i coefficients themselves must be wavenumber-independent. In practice two or three independent but contiguous altitude ranges are used to cover the total range between 80 km and the effective top of the atmosphere (~400 km, say), leading to two or three exponential expressions, requiring different values of c_i, being pieced together to cover the entire range.

If the chemical time constant associated with the formation rate of the aerosol is significantly smaller than the dynamical time constant associated with atmospheric turnover, the chemical composition of the aerosol may vary with altitude. We allow for this by adding a second aerosol component with a different vertical distribution to the system.

In addition to the photochemical aerosol, Fig. 1 indicates there is a relatively narrow altitude range (between 50 and 90 km or so) where condensations of various hydrocarbons and nitriles are likely. Because this range is quite narrow compared with a typical FP1 field-of-view (FOV), a simple Gaussian

$$N\chi_v = N\chi_{0v} exp^{-0.5\left(\frac{z-z_0}{\sigma}\right)^2} \tag{5}$$

should be adequate to describe the vertical distribution of an associated ice cloud, where z_0 is the altitude of maximum abundance and σ defines the effective thickness of the cloud.

Finally, the Gas Chromatograph/Mass Spectrometer (GCMS) instrument aboard the Huygens Probe indicated that methane vapor was nowhere strongly supersaturated in Titan's lower atmosphere at 10°S latitude (Niemann et al., 2005), even though Courtin et al. (1995) and Samuelson et al. (1997) independently inferred methane abundances exceeding 150% of saturation in low-latitude regions of the upper troposphere. Both Courtin et al. and Samuelson et al. used the CIA coefficients for N_2–CH_4 and CH_4–CH_4 determined by Borysow and Tang (1993) and Borysow and Frommhold (1987).

It is now believed that these coefficients may be systematically in error, most probably in regions where temperatures are near those of CH_4 saturation, and thus where phase changes are likely. We therefore adopt a correction factor CF_v for N_2–CH_4 CIA coefficients:

$$CF_v = 1 + \left[\frac{\beta_v}{(T - T_{sat})^2 + \delta t}\right], \tag{6}$$

where T and T_{sat} are air temperature and CH_4 saturation temperature over ice, respectively, and where β_v and δt are free parameters; the former is a function of wavenumber, while the latter is not. The magnitude of δt narrows or broadens the altitude range over which β_v is effective.

The factor CF_v in Eq. (6) is to be used as a multiplier to known N_2–CH_4 CIA coefficients. The equation is strictly heuristic in the sense that it is neither derived from basic physical principles nor inferred from laboratory data. Instead it is a device for steadily increasing departures from published methane CIA coefficients as the local atmospheric temperature approaches that for methane saturation, where we believe errors in the calculations of these coefficients are most likely.

In summary, the general problem of inferring absorption coefficients for Titan's particulates has been cast in a form that emphasizes the physical structures expected. The quasi-uniformly mixed nature of the aerosol and the highly layered structure expected for stratospheric ices are indicated by Eqs. (4) and (5), respectively. A heuristic approach for including corrections to N_2–CH_4 CIA is given by Eq. (6). Solutions for the free parameters in these equations are then derived from nonlinear least-squares fits of radiative transfer solutions to CIRS data in the wavenumber range 20–560 cm^{-1}.

3. Instrumentation and observations

The CIRS instrument consists of two interferometers that share a single telescope and scan mechanism (Flasar et al., 2004). One interferometer contains focal planes FP3 and FP4, each of which is associated with a 10-element linear array of detectors. FP3 is sensitive to a mid-IR spectral range of 600–1100 cm^{-1}, while FP4 is sensitive over 1100–1400 cm^{-1}. The FOV of each element in both arrays is a square, 0.273 mrad on a side, projected onto the plane of the sky.

The second interferometer includes a single-element FIR focal plane, FP1, sensitive to the spectral range 10–600 cm^{-1}. Its FOV is circular, with decreasing sensitivity from the center (at 0 mrad)

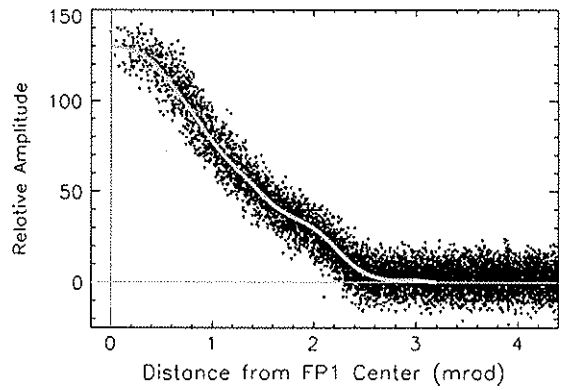

Fig. 2. Relative amplitude of FP1 FOV sensitivity function. Solid black stars are normalized spectrally integrated fluxes of Jupiter, recorded by CIRS in an October 2001 flyby of Jupiter, when Jupiter's disk was small relative to the FOV. The solid orange curve is the best fit to the Jupiter measurements, showing an FOV intensity that drops to zero at the 3.2 mrad detector edge. (For interpretation of the references to colour in this figure legend, the reader is referred to the web version of this article.)

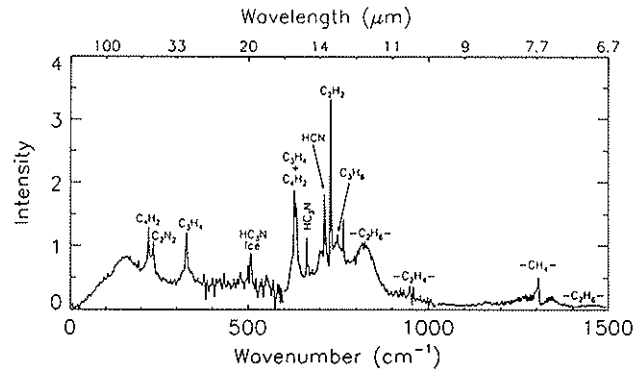

Fig. 3. CIRS spectrum of the limb of Titan at 62°N. Spectral resolution is 3.0 cm^{-1}. Many emission features of both hydrocarbon and nitrile vapors are evident, as well as one feature of HC_3N ice at 506 cm^{-1}.

to the edge, 3.2 mrad from the center, where the sensitivity drops to zero. The sensitivity function was determined from scans of Jupiter crossing the FOV during the Jupiter flyby when the image of Jupiter was small compared with the FOV. Signal-to-noise was maximized by treating the interferometer as a radiometer (integrating over all wavenumbers). Results are shown in Fig. 2, and replace an earlier version found in Flasar et al. (2004). It is necessary to take the spatial FOV characteristics into account wherever data from the limb of Titan are analyzed because spatial convolution of the model is required in these cases.

A wealth of aerosol and stratospheric ice information is contained in FP1 data. Fig. 3 illustrates a CIRS composite spectrum at 62°N comprised of data across all three focal planes, and identifies the known gases, condensates, and some of the unidentified spectral features in Titan's thermal infrared spectrum. The continua in FP3 and FP4 are defined by the aerosol, with gas emission features

Table 1
FIR limb aerosol scans ($\Delta\nu = 15.5 cm^{-1}$).

Titan encounter	Date	Latitude	$R_{avg}(10^3$ km)	H (km)
T6	22 August 2005	58S	21.0	−95 to 713
T17	07 September 2006	15S	22.5	−101 to 564
T26	10 March 2007	15N	21.5	−54 to 742

superimposed on the continuum. Although FP3 is crowded by strong gas emission, the spectral range 1050–1150 cm^{-1} in FP4 is completely free of these features and the signal from aerosol opacity is evident. The FP1 continuum on the other hand, is relatively free of gas emission features, and is defined by a combination of opacity from aerosol, CIA, and broad ice emission features in Titan's lower stratosphere.

There are two data acquisition modes that we utilize in the analyses at latitudes 15°N, 15°S, and 58°S. The first mode with which we are primarily concerned is a limb-scan sequence where the FP1 FOV center nominally begins 650 km above the solid-surface horizon of Titan as seen from Cassini and scans slowly across the limb of Titan to a point about 100 km below the horizon. This data mode is especially important for inferring vertical distributions of aerosols and stratospheric ices, especially for ices with broad emission features that blend into the aerosol continuum and are otherwise difficult to detect. The spectral resolution is 15.5 cm^{-1}, and the time required to acquire a single spectrum (interferogram) is about 5 s. The duration of a single scan is typically 30 min, and thus consists of about 360 individual spectra contiguously distributed in height above and below the limb. The second data acquisition mode (sit-and-stare) involves spectral averages acquired in a limb-integration sequence in which the FP1 FOV is restricted to a single tangent height on the limb at a given latitude. Spectral resolution is 0.5 cm^{-1}, and time of acquisition for a single spectrum is about 50 s. This mode is particularly important for ice identifications with strong and narrow emission features, and for determinations of the thermal structure in the lower stratosphere using the pure rotation lines of CH_4 between 80 and 145 cm^{-1} (see Section 5). Typically 12 spectra or so are averaged over a 10 min observing sequence, although many sequences are longer. Tables 1 and 2 list the observations taken in both data acquisition modes.

4. Opacity sources

There are four categories of opacity sources that we account for in our atmospheric model (Sections 5, 6); these include: aerosol, stratospheric condensates, gas emission features, and CIA. Each source of opacity tends to influence a different altitude region in Titan's atmosphere. Aerosol opacity contributes everywhere in altitude, latitude, and longitude. Ice opacity is restricted to narrow altitude regions in the lower stratosphere where condensation is expected to occur. Ices should form where vapor pressures reach 100% of saturation. Gas emission is limited to altitude regions higher up in the stratosphere and mesosphere; the gases are removed in the lower stratosphere by condensation. CIA is dominant in the troposphere. CIA has a pressure-squared opacity dependence

Table 2
FIR sit-and-stare limb-integrations ($\Delta\nu = 0.5 cm^{-1}$).

Titan encounter	Date	Latitude	$R_{avg}(10^3$ km)	Center FOV z (km)	# of spectra in average
T6	22 August 2005	55S	39	123; 132	23; 25
T17	07 September 2006	15S	39	119	16
T26	10 March 2007	10N	39	124	19

so that the scale heights are only about half those of other gases. Fig. 1 gives an illustrative sense of the altitude location of these continuum (aerosol) and quasi-continuum (CIA and ice) sources, apart from emission features due to gases.

C_4H_2, C_3H_4, and HC_3N line intensities are taken from the GEISA 2003 line atlas (Jacquinet-Husson et al., 2005); CO and HCN line intensities are taken from the HITRAN 2004 line atlas (Rothman et al., 2005); and CH_4 rotational line intensities are taken from Boudon et al. (in press). All line lists are included in converting to the correlated-k approximation of Lacis and Oinas (1991).

A uniform stratospheric CH_4 mole fraction of 1.41×10^{-2} is assumed as inferred from the Huygens GCMS (Niemann et al., 2005); reasons for expecting uniform mixing of CH_4 throughout Titan's stratosphere have been given by Dire (2000). The vertical distribution of CH_4 below the stratosphere follows the GCMS profile. The mixing ratio of CO is held uniform with height at 50 ppm. We pattern the vapor vertical profiles of HCN and HC_3N after Teanby et al. (2007) and C_4H_2 and C_3H_4 after Vinatier et al. (2007). The H_2 mole fraction of 0.112% is uniformly distributed (Samuelson et al., 1997); the ortho/para ratio is assumed to be in thermodynamic equilibrium (Conrath and Gierasch, 1983).

The most important tropospheric opacity sources in the thermal infrared are due to CIA. We include CIA contributions from seven pairs of molecules: N_2–N_2, N_2–CH_4, CH_4–CH_4, N_2–$H_{2,para}$, N_2–$H_{2,ortho}$, CH_4–$H_{2,para}$, and CH_4–$H_{2,ortho}$ (Borysow and Frommhold, 1986a,b,c, 1987; Borysow and Tang, 1993). The normal atmospheric optical thicknesses for all seven pairs are illustrated in Fig. 4, highlighting the magnitude and wavenumber dependence of each pair. For wavenumbers shortward of ~150 cm^{-1}, N_2–N_2 CIA dominates the tropospheric opacity, but for wavenumbers longward of 150 cm^{-1}, N_2–CH_4 CIA is the dominant tropospheric opacity source (Samuelson et al., 1997). Employing the same CIA coefficients that are used in this current work, Courtin et al. (1995) and Samuelson et al. (1997) had difficulty fitting Voyager IRIS spectra in the troposphere, and found it necessary to supersaturate CH_4 in order to obtain good fits with the data. However, *in situ* measurements from the Huygens GCMS strongly imply that Titan's tropospheric methane is not supersaturated at latitude 10°S. If the CH_4 abundance and CH_4 clouds (see Section 7) are not responsible for the required extra opacity in Titan's troposphere, then most likely the nominal N_2–CH_4 CIA coefficients are

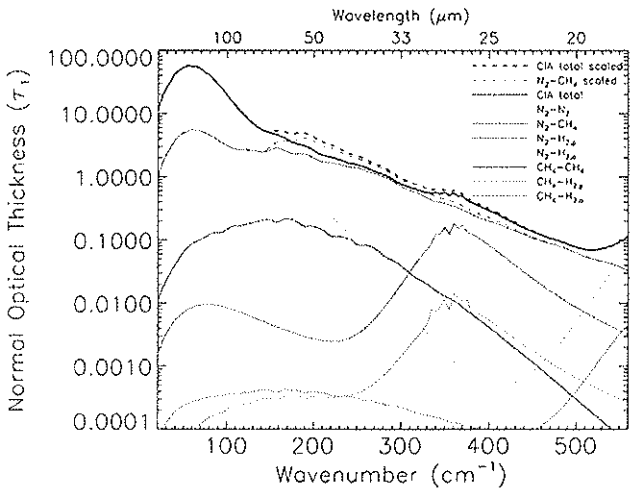

Fig. 4. Normal optical thicknesses of Titan's atmosphere at 15°S due to collision-induced absorption (CIA). Contributions from seven molecular pairs are shown separately, as well as the total. Para ($H_{2,p}$) and ortho ($H_{2,o}$) molecular hydrogen are considered individually. Corrections to nominal N_2–CH_4 CIA, as well as the total, are shown by dashed curves, and are derived empirically from Eq. (6).

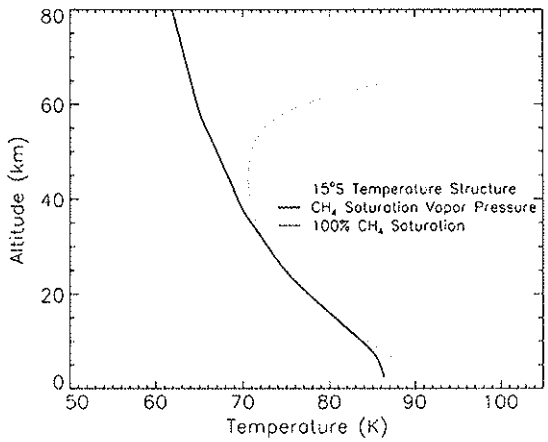

Fig. 5. Temperature profile (thin curve) and methane saturation vapor pressure (thick curve) over ice for 15°S latitude. The pink portion of the saturation curve indicates the altitude range over which CH_4 condensation can occur and corrections to nominal N_2–CH_4 CIA become maximum (see Eq. (6)). (For interpretation of the references to colour in this figure legend, the reader is referred to the web version of this article.)

incorrect. We attempt to introduce the necessary corrections through Eq. (6).

Fig. 5 depicts the relationship between Titan's temperature structure and the CH_4 saturation vapor pressure vertical profile at 15°S. For temperatures $\geqslant$90.79 K, we use the CH_4 vapor–liquid pressure expression of Angus et al. (1976), and for temperatures <90.79 K we use the CH_4 vapor–ice pressure expression from Armstrong et al. (1955). A comparison of Fig. 5 with Eq. (6) suggests that maximum departures from nominal N_2–CH_4 CIA most likely occur between altitudes of 15 and 30 km.

5. Temperature structure at 15°N, 15°S, and 55°S

Above about 3 mbar (~160 km), we adopt the temperature structures of Achterberg et al. (2008) derived from the CIRS FP4 ν_4 CH_4 emission feature at 1306 cm^{-1}. Achterberg et al. apply a constrained linear inversion technique to derive vertical thermal structure between ~5 and 0.2 mbar from CIRS nadir maps at 3 cm^{-1} spectral resolution, and between 1 and 0.005 mbar from CIRS limb observations at 15.5 cm^{-1} spectral resolution. 1σ uncertainties over this entire altitude range tend to be less than 2 K.

For 15°S and 15°N latitudes, we impose the Huygens Atmospheric Structure Instrument (HASI) temperature structures at altitudes below ~160 km. Where we depart significantly from latitudes relatively close to the Huygens descent latitude of 10°S (*i.e.* 55°S), we can no longer apply the HASI temperature profile at all altitudes below 160 km. Aerosol opacity begins to play a more dominant role, and thermal structure from the CH_4 ν_4 band can no longer be determined without taking the aerosol into account. In addition to the HASI profile, the strength of the FIR pure rotation lines of CH_4 between 80 and 145 cm^{-1} can be used to infer temperature at some level in the pressure region between 3 and 30 mbar (~80 and 160 km). This is where CIRS sit-and-stare limb spectral averages are obtained at 0.5 cm^{-1} spectral resolution at a specific limb-tangent height (*e.g.* 125 km) above the solid-surface horizon as seen from Cassini. The continuum can be observed between individual CH_4 lines. Radiative transfer calculations demonstrate that the continuum opacity from particulates is optically thin enough that any physical mechanism (in addition to CIA) which provides the correct continuum intensity is acceptable.

With the assumption of a constant CH_4 mole fraction of 1.41% throughout the stratosphere, the observed strengths of the rotation

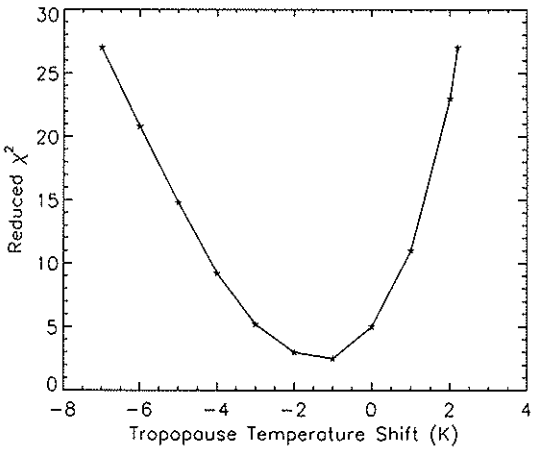

Fig. 6. Chi-squared merit function for the derived tropopause temperature difference T_t(55°S)–T_t(15°S) at the indicated latitudes.

lines of CH_4 relative to the continuum yield unique temperatures, independently of the physical nature of the aerosol contribution to this continuum. 1σ uncertainties can range from about 2 K at low latitudes to as much as 10 K at very cold high northern latitudes, where the lines are especially weak (see Anderson et al., 2010).

The opacity near 200 cm^{-1} due to CIA of N_2–N_2 and N_2–CH_4 is very high near the tropopause (altitudes ~ 40 km; pressure ~ 100 mbar), and the atmosphere is basically isothermal there. Flasar et al. (1981) and Samuelson et al. (1981) demonstrated from Voyager 1 IRIS data that under these conditions the tropopause temperature T_t can be inferred to within a kelvin or two, regardless of the exact nature of the tropopause opacity. Later, Samuelson et al. (1997) mapped T_t from IRIS data as a function of latitude. CIRS limb-scan data can improve determinations of the tropopause temperature. In addition to parameters defining the optical and distributional properties of Titan's ices and aerosols, we include T_t as a parameter in the *Levenberg–Marquardt* least-squares analysis (Section 7) of limb-scan data. Results demonstrating the functional dependence of the χ^2 merit function [Eq. (3)] on T_t at 55°S are portrayed in Fig. 6, and confirm that, because of the sharpness of the minimum, a rather precise determination of T_t is possible, independently of aerosol and ice properties. We find the tropopause temperature at 55°S to be 69.3 K, 1.2 K cooler than the HASI tropopause temperature of 70.5 K.

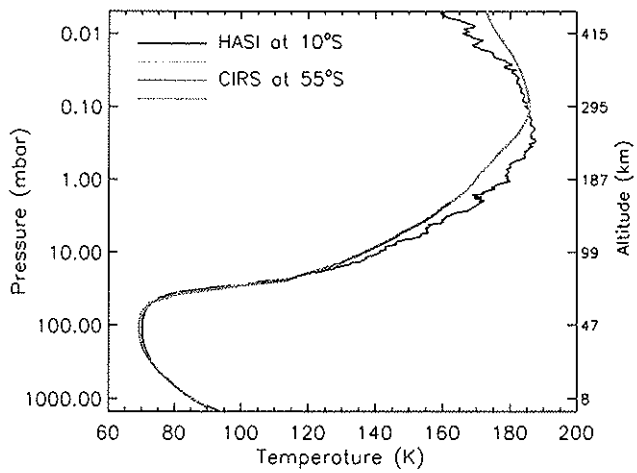

Fig. 7. Temperature profile at 55°S. The HASI profile at 10°S is shown for comparison. The upper (green) section of the CIRS profile is determined from inversion of the 1306 cm^{-1} band of CH_4 (Achterberg et al., 2008). The lower section (blue) is inferred from scaling the shape of the HASI profile to include two independently determined points at the tropopause and surface (Samuelson et al., 1997). The middle section (pink) is an interpolation between the other two sections, constrained to include a point derived from CH_4 rotation lines between 80 and 145 cm^{-1} (Samuelson et al., 2007). (For interpretation of the references to colour in this figure legend, the reader is referred to the web version of this article.)

We adopt the 15°N and 55°S surface temperatures from Jennings et al. (2009) with 1σ uncertainties of 1–2 K. Interpolations for temperatures between 80 km, the tropopause, and the surface, where the temperature has been well-determined, are then derived by retaining the general shape of the HASI profile at 10°S across the regions where interpolation is required. This procedure is patterned after Samuelson et al. (1997). Interpolations that require retaining the general shape of the HASI profile are restricted to regions in the lower, denser portions of the atmosphere, where thermal time constants are long compared with a season, and thus where deviations of temperature profile shape with time are not expected.

The resulting temperature profile for 55°S is shown in Fig. 7, and extends from the surface to the 0.005 mbar level. The solid black curve is the HASI temperature profile at 10°S and the different color segments constitute our derived temperature profile at 55°S for altitudes above 160 km (green curve), altitudes between 80 and 160 km (pink curve), and altitudes below 80 km (turquoise curve).

6. Model implementation

Even though, in the aerosol limb-scan mode, the FP1 FOV full diameter of 6.4 mrad is equivalent to between 130 and 150 km when projected onto the limb of Titan, the slow scan rate across the limb (about 1–5 km per interferogram) enables a much smaller effective vertical resolution. How much smaller depends critically on the signal-to-noise ratio, and this varies strongly with wavenumber. Successive interferograms overlap by between 95% and 99%.

The process for fitting the aerosol limb-scan data can be outlined with a simplified procedural model. Consider a particulate medium consisting solely of a diffusely distributed single-component aerosol and a single vertically compact stratospheric ice cloud, as illustrated in Fig. 1. Divide the atmosphere vertically into four altitude ranges z_i: ($i = 1$), 500–220 km; ($i = 2$), 220–160 km; ($i = 3$), 160–80 km; ($i = 4$) 80–0 km. Begin at an altitude where the atmosphere does not emit signal and scan slowly down until sufficient data have been acquired to solve for $N\chi_{01\nu}$ and c_1 in Eq. (4) separately at each wavenumber in the range 20–560 cm^{-1}. The *Levenberg–Marquardt* nonlinear least-squares procedure solves for $N\chi_{01\nu}$ and c_1 automatically. Average over wavenumber to obtain a wavenumber-independent value of c_1.

Using this fixed value of c_1 (over range $i = 1$), repeat, in order, for altitude ranges 2, 3, and 4, making sure that the $N\chi_{0i\nu}$ are contiguously connected across each altitude range boundary. At some point the ice cloud will influence the opacity, and the parameters $N\chi_{0\nu}$, z_0, and σ in Eq. (5) must then be included as parts of the least-squares solution. Because the aerosol spectral properties are fairly well defined at this point, solutions for the ice cloud parameters tend to separate readily from those of the aerosol.

Solutions for β_ν in Eq. (6) can be retrieved uniquely, primarily because CIA opacity variations with altitude are significantly different from those of both aerosol and ice. We find through experience that setting $\delta_t = 1.0$ in Eq. (6), where T and T_{sat} are in kelvin, works well. A final minor iteration for $N\chi_{0\nu}$ in Eqs. (4) and (5) leads to our end results.

Solutions for more complicated models, such as those including two-component aerosol systems, are obtained using similar procedures. As a rule, models containing three or more particulate

components in the stratosphere lead to non-unique solutions if two or more components are aerosols.

Exceptions can occur under special conditions. For example, solutions for a composite consisting of a one-component aerosol and two ice clouds can sometimes be determined uniquely, provided both the spectral and spatial characteristics of the two ice clouds are sufficiently separable.

It should be emphasized that solutions for the opacities of each component at a given latitude are determined independently at each wavenumber, subject to the condition that each component has a unique vertical distribution at that latitude that is wavenumber-independent (as it must be; see Section 2). Thus we solve for the spectral characteristics of each component separately for each data set. This enables us to determine the latitudinal dependences of both the spectral and spatial characteristics of each component, whether aerosol or stratospheric ice.

Accurate vertical profiles can be compromised by pointing uncertainties (see *e.g.* Vinatier et al., 2007). In practice, as indicated in the next section, we are always able to fit data sets satisfactorily without vertical adjustments to these sets. Hence we have neither a need nor a ready procedure for correcting any such possible pointing errors.

7. Results

Solutions for particulate properties at 15°S latitude will be considered first. The temperature profile is well defined at this latitude (Section 5), which is near the latitude of the Huygens descent probe (10°S). Aerosol limb-scan intensity profiles at several equally spaced wavenumbers are shown in Fig. 8. The data extend from a limb tangent height $h = 564$ km above the solid surface to $h = -101$ km below it. Intensities from individual spectra are plotted as pink dots, and successive points are connected with straight lines. The resulting curves demonstrate the relative noise at each wavenumber.

For a specific wavenumber, the signal is zero at the top of the atmosphere, indicating no atmospheric opacity. As the FOV descends in tangent height, the intensity first increases rapidly as a result of increasing density, and then changes character as the temperature becomes relatively more important in defining the signal. Below a tangent height of zero the center of the FOV is on the disk. In this region, the slope of the curve indicates limb brightening if positive, or limb darkening if negative. Radiation originates dominantly from the stratosphere in the former case, and from the troposphere in the latter.

A particulate model consisting of a single-component aerosol and a relatively thin ice cloud appears most consistent with the data at 15°S. The solid black curves in Fig. 8 are best fits to the data for this model in the least-squares sense. In practice we compute tangent-height intensity profiles every five wavenumbers. The fits tend to be quite good over the entire tangent height range at wavenumbers above 80 cm^{-1}. Below 80 cm^{-1}, however, the fits become steadily worse as wavenumber decreases. On the other hand, large reductions below nominal values for N_2–N_2 CIA coefficients enable significantly better fits at wavenumbers below 80 cm^{-1}.

Aside from possibly incorrect N_2–N_2 coefficients, which may play a significant role, we also suspect that part of the problem may be due to faulty instrument calibration. Determination of

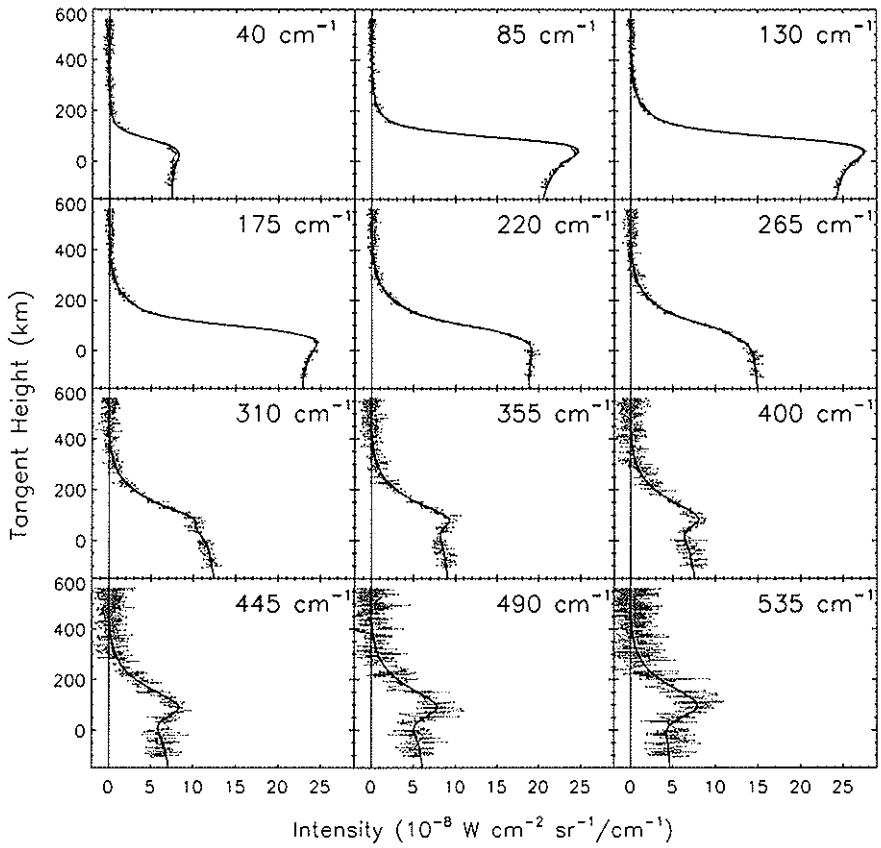

Fig. 8. Observed (pink) intensity vs. tangent height profiles at 12 individual evenly spaced wavenumbers at 15°S latitude. Individual points represent single spectra; contiguous points are connected with straight lines. Tangent heights are positive above Titan's solid-surface limb, and negative below. Least-squares fits to the data for a single-component aerosol plus ice cloud model are illustrated by the solid black curves. In practice, fits are made every 5 cm^{-1}, covering a spectral range 20–560 cm^{-1}. (For interpretation of the references to colour in this figure legend, the reader is referred to the web version of this article.)

the FP1 FOV sensitivity curve shown in Fig. 2 depends on using the CIRS instrument as a radiometer, and the curve is assumed to be independent of wavenumber. If this is incorrect at low wavenumbers, deviations from good fits will result. For example, Fig. 9 shows how different effective FOV diameters affect the shapes of the fits. We speculate that distortions of both FOV size and shape may occur at the lowest wavenumbers, leading to less reliable results than those associated with wavenumbers above 80 cm^{-1}.

Vertical distributions of the derived opacity at 160 cm^{-1} for both aerosol and ice cloud are shown in Fig. 10. Because aerosol particle radii are so much smaller than the wavelength of radiation ($\lambda = 62.5$ μm), the aerosol opacity distribution is directly proportional to abundance distribution (see *e.g.* McKay et al., 2001). Solutions are compatible with a constant volume absorption coefficient below 80 km. The mass absorption coefficient (and hence mass mixing ratio) would be independent of altitude if the aerosol were uniformly mixed. Thus the observed positive gradient for the mass absorption coefficient is compatible with a strong aerosol source above 300 km and an effective sink below 80 km.

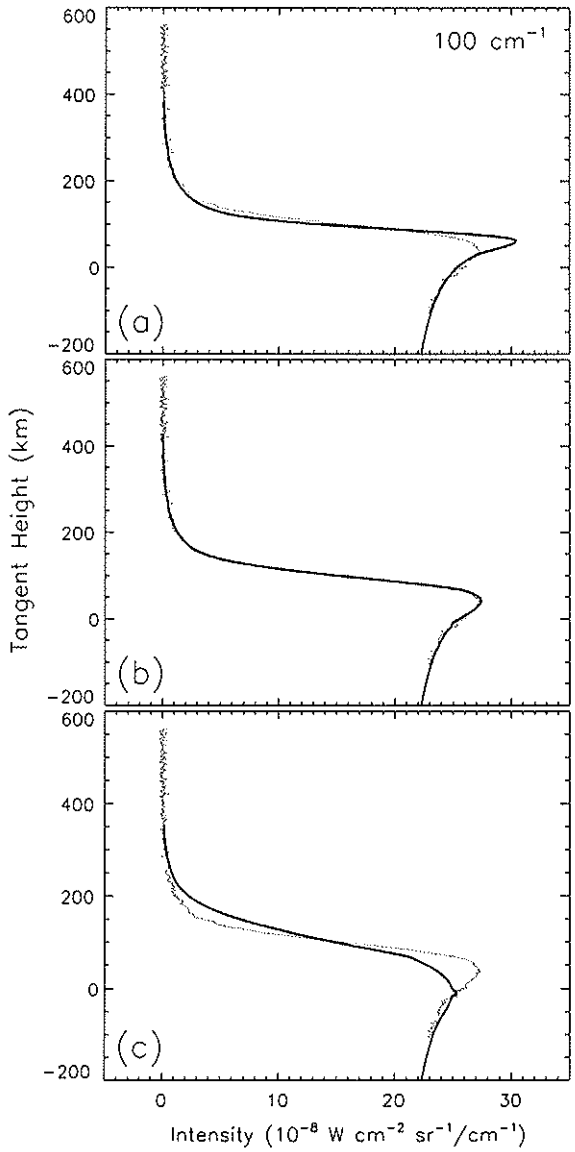

Fig. 9. Effect of FOV size on least-squares fits to intensity profile at 100 cm^{-1} at 15°S. Nominal FOV size is determined from the known range of the spacecraft to Titan at the time of observation. Relative sizes are indicated in the three panels as follows: (a) one-half nominal size, (b) nominal size, and (c) twice nominal size.

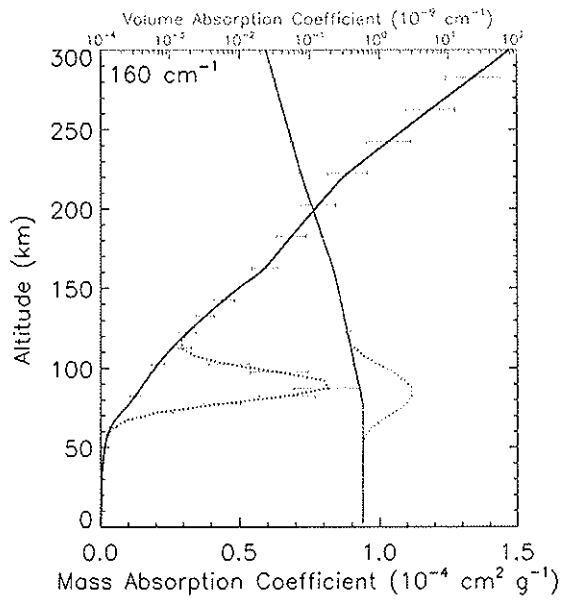

Fig. 10. Derived vertical distributions of mass absorption coefficient (black) and volume absorption coefficient (pink) at 160 cm^{-1} at 15°S. The model assumes a single aerosol and a single ice cloud component. Absorption coefficients are for aerosol only (solid curves) and aerosol plus ice (dotted curves). 1σ uncertainties are also shown. (For interpretation of the references to colour in this figure legend, the reader is referred to the web version of this article.)

An additional source of opacity, which we identify with an organic ice cloud, is restricted in thickness to 40 km or so, and is centered at an altitude of about 90 km. The location is consistent with where condensations of organic vapors (especially nitriles; see Fig. 1) are expected.

Derived volume absorption coefficient spectra for both aerosol and ice at 15°S, for an altitude of 77.5 km (aerosol) and 67.5 km (ice), are shown in Fig. 11. The main spectral characteristics of the aerosol absorption coefficient are: (1) a general monotonic decrease in magnitude from high to low wavenumbers, except for (2) a very broad and relatively strong absorption feature centered roughly at 140 cm^{-1}. Ice cloud opacity, on the other hand, appears to be restricted to a single, broad feature between 80 cm^{-1} and

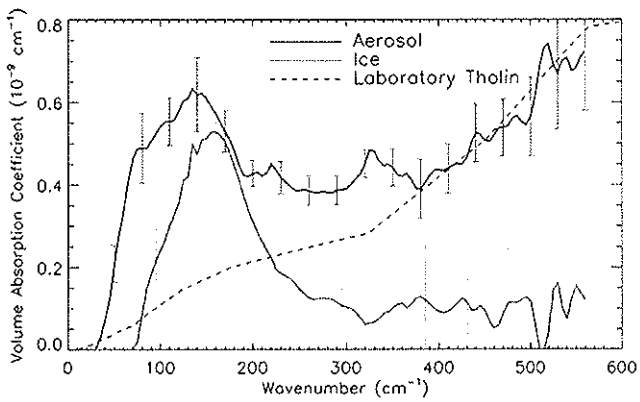

Fig. 11. Derived spectral variations of absorption coefficients of aerosol (black) and ice cloud (pink) at an altitude of 77.5 km and 67.5 km, respectively, for the model shown in Fig. 10. 1σ uncertainties are also shown. The dashed black curve is derived from the Khare et al. (1984) laboratory measurements of simulated Titan aerosol (tholin) in the small particle limit. (For interpretation of the references to color in this figure legend, the reader is referred to the web version of this article.)

280 cm^{-1} or so, peaking at about 160 cm^{-1}. For comparative purposes, the spectral variations of the Khare et al. (1984) Titan tholins (laboratory-created aerosols) are indicated by the dashed black curve as computed from the small particle limit of the Mie theory. The spectral dependence between Titan's aerosol and laboratory-created tholins agree between 400 and 600 cm^{-1} but there is an increasing discrepancy shortward of 400 cm^{-1}; this is due to chemical bonds associated with Titan's aerosol that laboratory measurements have as yet not reproduced.

The magnitudes of both ice and aerosol spectra are strong functions of altitude; the shapes, however, are height-independent. Thus, within limitations of the data, the chemical nature of the aerosol appears invariant between the surface and the top of the stratosphere at 15°S.

A 0.5 cm^{-1} spectral resolution sit-and-stare spectral average at 15°S is illustrated in Fig. 12. There are 16 spectra in the average, and the center of the effective FOV is at an average tangent height of 119 km. The solid black curve is our predicted spectrum for these conditions, and fits the data quite well. Vapor abundances are adopted from Teanby et al. (2007) and Vinatier et al. (2007), and the contribution to the continuum by particulates is derived from the aerosol and ice cloud properties shown in Figs. 10 and 11. The resulting comparison demonstrates internal consistency, and implies our model is consistent with actual conditions in Titan's atmosphere.

The continuum contribution by CIA includes the modifications to N_2–CH_4 CIA indicated by Eq. (6). Solutions for β_ν in Eq. (6) are illustrated in Fig. 13. As discussed in Section 2, CH_4 supersaturation should yield the same wavenumber dependence for additional opacity as β_ν. In fact, the wavenumber dependence of β_ν between 200 and 560 cm^{-1} is consistent with that inferred for methane supersaturation from IRIS spectra by Samuelson et al. (1997); checks are not available below 200 cm^{-1}. Because β_ν is included as a parameter in all least-squares fits to aerosol limb-scan data, the aerosol and ice cloud characteristics we have derived include its effect as well.

We have tried other model forms to test for uniqueness. Models containing a two-component aerosol plus an ice cloud fail to converge. Partial results are chaotic, and uniqueness of solution is impossible. If the ice cloud is removed from this model, one of the aerosol components attempts to reproduce the vertical distribution characteristics of the layered cloud. This is possible if enough c_i-

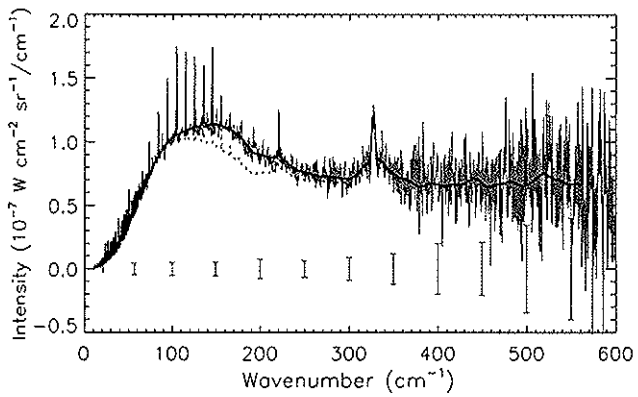

Fig. 12. Sit-and-stare average of 16 spectra on the limb of Titan at 15°S at a tangent height of 119 km (pink curve). Spectral resolution is 0.5 cm^{-1}. The solid black curve is a corresponding spectrum calculated from our one-component aerosol plus ice cloud model at 15°S. The model spectrum is not a fit to the observed spectrum, but rather is calculated independently, and serves as a consistency check. The dotted black curve is the solid black curve minus the ice contribution. 1σ uncertainties are indicated by the pink error bars below the data at zero intensity. (For interpretation of the references to color in this figure legend, the reader is referred to the web version of this article.)

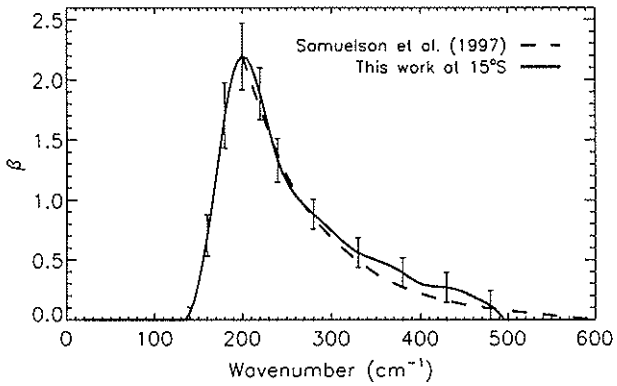

Fig. 13. Functional dependence of β_ν in Eq. (6) on wavenumber at 15°S (solid curve), with δ_t = 1.0. Also shown for comparison (dashed curve) is the wavenumber dependence of the excess opacity needed in Titan's troposphere to fit Voyager 1 IRIS spectra if methane supersaturation is not allowed (Samuelson et al., 1997). Both curves are primarily measures of deviations from nominal theoretical unsaturated N_2–CH_4 CIA calculations (Borysow and Tang, 1993), and as such should be qualitatively similar. Samuelson et al. extra opacity curve is scaled by a factor of 1.1.

factors are included in Eq. (4) so that the vertical distribution shape can roughly mimic the shape defined by Eq. (5). Fits to the data are decent, but the ice cloud layer becomes reestablished with about the same spectral characteristics as before, even though we initially consider it to be a second aerosol component.

If we force the vertical distributions of both aerosol components to resemble the shape of the vertical distribution of the aerosol in Fig. 10, thereby eliminating any effects due to a cloud layer, the fits become unacceptable at many wavenumbers, especially in the spectral region containing the main ice feature shown in Fig. 11. Comparisons of this two-component aerosol model with our derived one-component aerosol plus ice model are shown in Fig. 14. Deficiencies in the two-component aerosol model (Fig. 14b) are clearly evident. Computed intensities are too high in the 150–300 km tangent height region, and too low in a 150 km tangent height range centered slightly above Titan's surface (h = 0). The introduction of an ice cloud centered at a tangent height of about 90 km, with a strong broad feature at ~160 cm^{-1}, appears mandatory in order to fit the data well (Fig. 14a).

Comparisons of the inferred ice feature at 160 cm^{-1} with laboratory spectra of HCN and HC_3N ices are shown in Fig. 15. Laboratory spectra for HCN and HC_3N obtained separately are shown in panel (a) (Moore et al., submitted for publication). Panels (b), (c), and (d) show spectra of ice composites deposited under different thermal and mole fraction ratio (HCN/HC_3N) conditions (M.H. Moore, personal communication).

Nitrile ices typically have strong features in this part of the spectrum that are due to lattice vibrations of the crystalline structure (Dello Russo and Khanna, 1996). This suggests the possibility that the aerosol absorption feature at ~140 cm^{-1} (see Fig. 11) may result from the same general physical cause. Instead of originating from a three-dimensional crystalline ice structure, however, this low-energy aerosol feature may be a composite resulting from low frequency vibrations of the two-dimensional lattice structures of large planar molecules such as polycyclic aromatic hydrocarbons (PAHs) and nitrogenated aromatics (see *e.g.* Ricca et al., 2001). Such molecules have been advocated as significant components of Titan's aerosol (*e.g.* Waite et al., 2007; see also Waite et al., 2009, for a review).

In addition to 15°S, we have completed analyses at latitudes 15°N and 58°S. A few particulars of the aerosol limb-scans used are contained in Table 1. Temperature profiles are discussed in Section 5. We analyze the 58 °S data using the nearby 55 °S temperature profile.

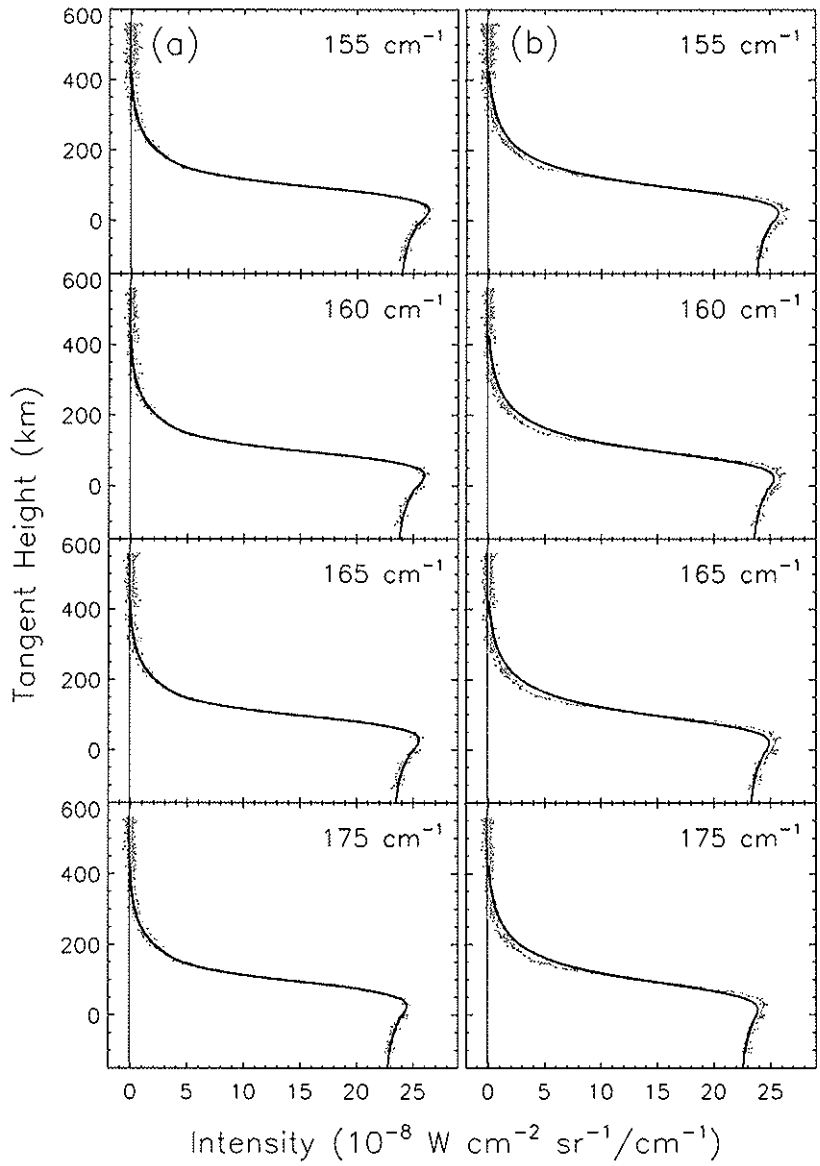

Fig. 14. Comparisons of model fits to intensity profiles at 15°S for: (a) one-component aerosol plus ice cloud model, and (b) two-component aerosol plus no ice cloud model.

Comparisons of the derived vertical distributions of both aerosol and ice for latitudes 15°N, 15°S, and 58°S are shown in Fig. 16. Corresponding spectral comparisons are indicated in Fig. 17. The most noteworthy results of the comparisons are: (1) the shape of the aerosol spectrum does not change significantly with latitude over the latitude range we have considered, and (2) both the spectral shapes and vertical distributions of the ice component do show changes. Excessive noise at the highest wavenumbers in Fig. 17c does not affect these conclusions.

The various kinks in the derived aerosol vertical distributions are largely functions of our procedure, and reflect the simplicity of the functional form of Eq. (4). Uncertainties within the error bars allow some smoothing. Even so, there is a tendency for the aerosol-to-gas scale height ratio to decrease with altitude in the stratosphere above 160 km. This is consistent with the results of Vinatier et al. (2010), who found a similar trend from the analysis of CIRS mid-IR spectra between 600 and 1420 cm^{-1}.

The broad aerosol emission feature at 140 cm^{-1} is quite real, and appears in all spectra. Smaller features at higher wavenumbers are probably all due to noise, which becomes steadily more severe above 300 cm^{-1} (see *e.g.* Fig. 8). The aerosol spectra at the various latitudes become different mainly below 80 cm^{-1}, where fits are poor; these differences therefore probably have little significance. We conclude that, within uncertainties in the data between 20 and 560 cm^{-1}, there is no evidence of a changing aerosol chemistry in the altitude range 0–300 km, and over a range of latitudes between 15°N and 58°S.

There appear to be definite changes in the ice component in going from low latitudes to 58°S. Although fits to the limb-scan data at 15°N and 15°S are acceptable for models with only one cloud layer, the same is not true at 58°S, where two cloud layers seem to be needed. A spectral feature centered at 170 cm^{-1} is associated with a layer at an altitude of 90 km or so, while another feature at ~80 cm^{-1} appears to be associated with a layer at ~60 km.

The need for two ice cloud layers at 58°S appears to be real. A comparison of one- and two-layer models is shown in Fig. 18. Least-squares fits to observed intensity profiles between 80 and 120 cm^{-1} indicate that, for the single-layer cloud model (Fig. 18a),

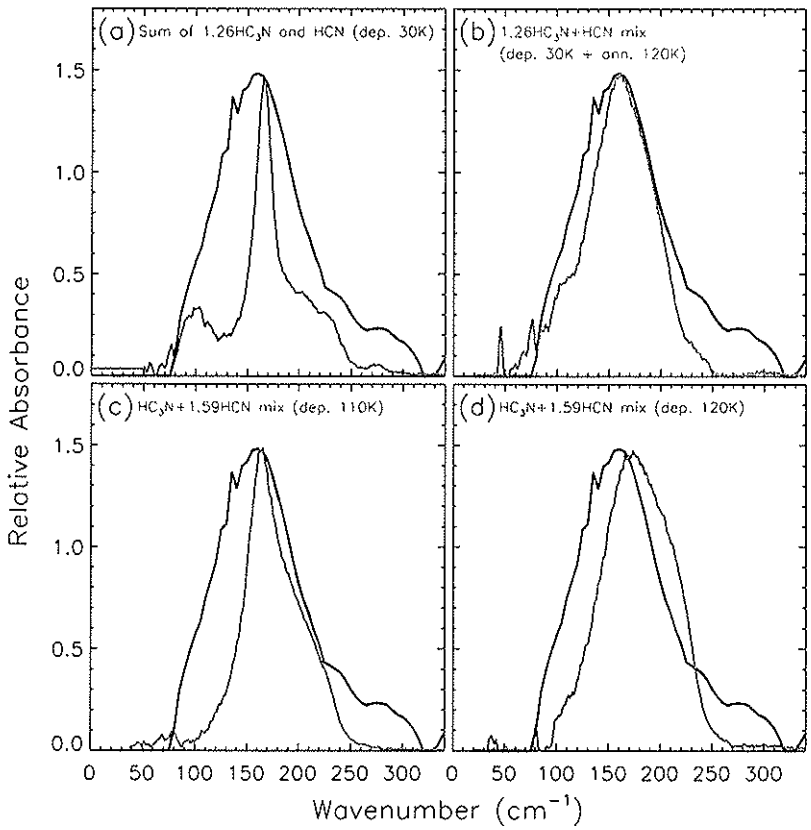

Fig. 15. Comparisons of ice cloud feature at 15°S (black curve) with absorbances of HCN and HC_3N ices determined under various laboratory conditions (colored curves). Absorbances are arbitrarily normalized. Conditions of deposition of HCN and HC_3N ice on cold finger before spectra are: (a) deposited separately at 30 K in the ratio HC_3N/HCN = 1.26; (b) deposited simultaneously as a mixture at 30 K in the ratio HC_3N/HCN = 1.26, annealed to 120 K, and cooled back down to 95 K; (c) deposited as a mixture at 110 K in the ratio HC_3N/HCN = 0.63; and (d) same as (c), except deposition temperature is 120 K ((Moore et al., submitted for publication), and personal communication). (For interpretation of the references to color in this figure legend, the reader is referred to the web version of this article.)

computed intensities are too low between tangent heights of +50 km and −25 km. Good fits are obtained at 58°S only for the two-layer model (Fig. 18b).

Both the spectral shape and altitude of the top layer appear to be consistent with nitrile ices and the altitudes at which they are expected to condense (Figs. 15 and 1, respectively). On the other hand, the altitudes at which hydrocarbon ices are expected to condense are more compatible with a layer at 60 km (see Fig. 1). Ethane (C_2H_6) ice is the likely candidate given that ethane in the vapor phase is the most abundant of any of the hydrocarbons (except methane). A comparison of the ice cloud feature at 80 cm^{-1} with laboratory spectra of C_2H_6 ice from Schwartz et al. (1971) suggests that C_2H_6 ice is indeed a possible candidate for this feature. Because of the great strength of the feature at 58°S and its total absence at 15°N and 15°S, it may be associated with a horizontally inhomogeneous cloud system.

Consistency checks of our results at 15°N and 58°S are provided by sit-and-stare spectral averages acquired at these latitudes (Table 2). Comparisons of models to the data are shown in Fig. 19. Like at 15°S, the models include our derived results for the particulate properties at 15°N and 58°S. The comparisons appear to be quite satisfactory, indicating our models are consistent with sit-and-stare spectra at 0.5 cm^{-1} spectral resolution.

8. Discussion

We regard the present study as an initial step in a more comprehensive investigation. We have limited ourselves to three latitudes for which both aerosol limb scans (at 15.5 cm^{-1} spectral resolution) and sit-and-stare sequences (at 0.5 cm^{-1} spectral resolution) are available, and for which reliable temperature profiles can be derived. The associated analyses are sufficient to determine several basic characteristics of Titan's photochemical aerosol and stratospheric ice cloud structures.

As illustrated in Figs. 11 and 17, both aerosol and ice have broad emission features located in and extending over very similar (though not identical) spectral regions. Because the features are so broad, we suspect each is a composite of several individual features. We have conducted a rather thorough analysis, and are fairly confident that, complex or not, two separate chemical systems are involved. No matter what our initial model conditions are, acceptable least-squares fits to the limb-scan data always yield vertical profiles of a well-mixed vertically extended aerosol component and a much more vertically compressed "ice" component located in the altitude ranges where condensations of organic vapors are expected in Titan's lower stratosphere.

Within uncertainties of the aerosol limb-scan data, the spectral shape of the derived aerosol component is independent of altitude, and different from the derived ice component. This is especially true at wavenumbers greater than 300 cm^{-1}, where the spectrum of the aerosol component, while noisy, is nevertheless quite strong, while that of the ice, discounting noise, is very weak.

A one-component aerosol is consistent with the CIRS limb-scan data at each of the three latitudes we have examined. In addition, the components at the three latitudes are spectrally almost identical. This suggests that the time constant associated with dynamical

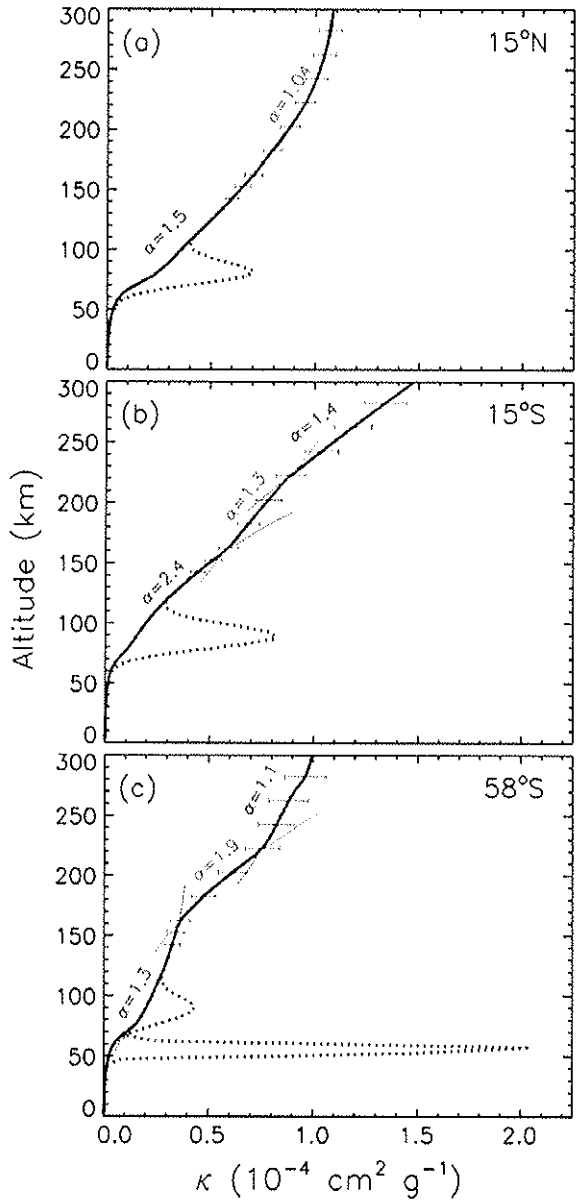

Fig. 16. Vertical distributions of the mass absorption coefficient at 160 cm^{-1} at: (a) 15°N, (b) 15°S, and (c) 58°S, for a one-component aerosol plus ice cloud model. The solid black curve is for aerosol only; the dotted black curve is for aerosol plus ice. A two-cloud system appears necessary at 58°S, involving different ices at separate levels. Absorption coefficient profiles for constant aerosol-to-gas scale height ratios α are shown as colored curves for different values of α. 1σ uncertainties are also shown. (For interpretation of the references to color in this figure legend, the reader is referred to the web version of this article.)

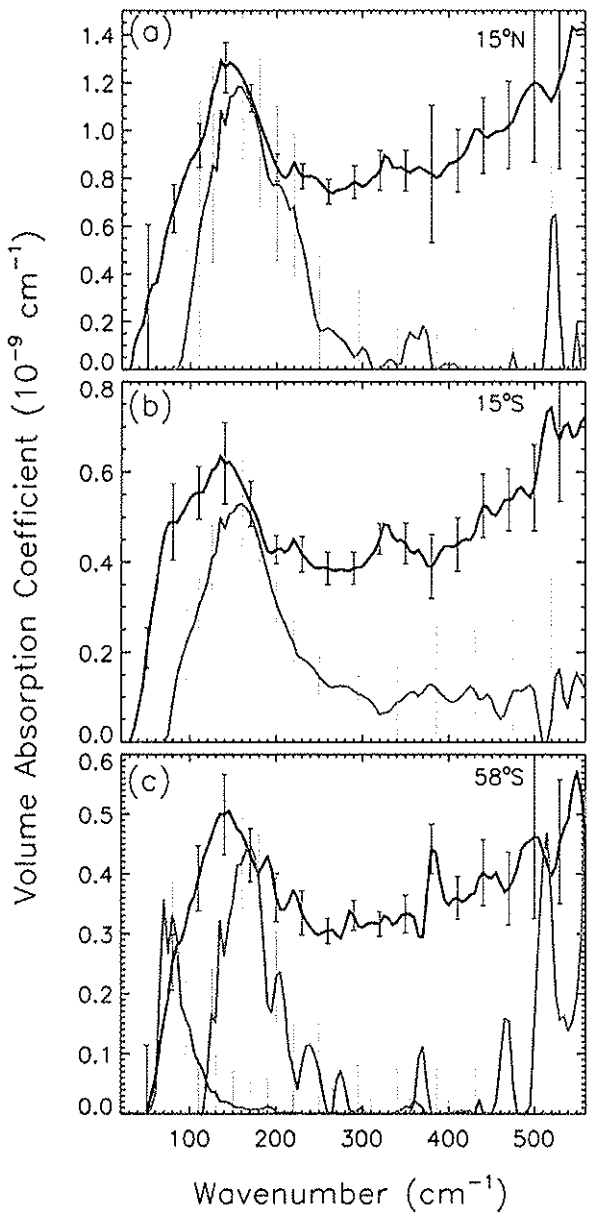

Fig. 17. Spectral variations of absorption coefficients of aerosol (black) and ice clouds (blue and pink) for the models shown in Fig. 11. Altitudes and latitudes for which calculations are shown are: (a) 15°N, 77.5 km (black solid line), 62.5 km (pink solid line) (b) 15°S, 77.5 km (black solid line), 67.5 km (pink solid line), and (c) 58°S, 107.5 km (black solid line), 72.5 km (pink solid line), and 67.5 km (blue solid line). The blue spectrum, peaking at 80 cm^{-1}, in panel (c) is associated with the cloud layer at ~60 km in Fig. 16c, whereas the pink spectrum, peaking at 160 cm^{-1}, is associated with the layer at ~90 km. 1σ uncertainties are also shown. (For interpretation of the references to color in this figure legend, the reader is referred to the web version of this article.)

overturning of the atmosphere is smaller than the time constant associated with the formation and chemical evolution of the aerosol, at least at these latitudes.

Conditions associated with the stratospheric ice cloud may be more complex. The spectral shape of the ice cloud feature changes shape with latitude, and is especially pronounced at 58°S (Fig. 17). Also, even though single layer ice clouds are adequate to fit the data at 15°N and 15°S, the fits are noticeably improved at 58°S between 80 and 120 cm^{-1} if two layers, separated by ~30 km and involving two separate chemical components, are included (Figs. 16 and 18).

At this time, we speculate that the upper layer at ~90 km is composed of nitrile ices ($HCN + HC_3N$ hybrid) and that the lower layer at ~60 km may consist of crystalline hydrocarbons (most likely ethane).

Unlike those for the aerosol, the spectral characteristics of the ice cloud composite vary with latitude between 15°N and 58°S. Two factors are probably involved. Firstly, latitudinal changes in temperature profile and vapor abundances (see *e.g.* Coustenis et al., 2007) will change corresponding condensation levels and relative ice abundances. Secondly, meridional circulation patterns of the atmosphere will modify and redistribute these ices. We make no attempt to explain the quantitative distributions at this time.

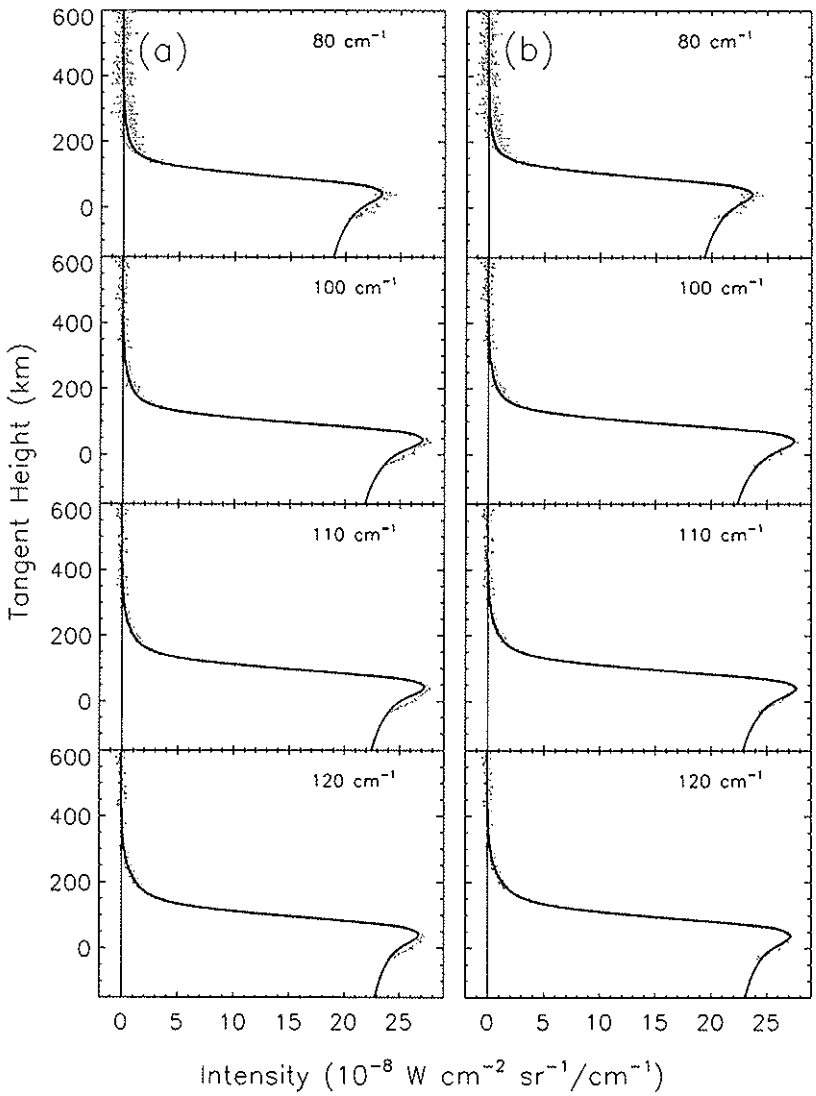

Fig. 18. Comparisons of model fits to intensity profiles at 58°S for: (a) a one-component aerosol plus one-layer ice cloud model, vs. (b) a one-component aerosol plus two-layer ice cloud model. Characteristics of the two-layer ice cloud model are shown in Figs. 16c and 17c.

The most active region for stratospheric ice cloud production is presently at northern high latitudes (de Kok et al., 2007; Samuelson et al., 2007; Anderson et al., 2010). We will conduct the next phase of our investigation there. As a preliminary step, we have fit, very roughly, a sit-and-stare average of 24 spectra at 62°N with a simplified model. The center of the effective FOV is at an altitude of 125 km, and the spectral resolution is 0.5 cm^{-1}. The temperature profile for the model is adopted from Anderson et al. (2010). Aerosol and ice characteristics are adopted from the present study at 15°S, except that the ice abundance is increased by a factor of three. Vapor abundances are taken from Teanby et al. (2007) and Vinatier et al. (2007).

The resulting continuum fit is displayed in Fig. 20, and is adequate for inferring approximate relative particle abundances; no attempt is made to include narrow emission features in the fit. There is no change of aerosol abundance compared with that at low latitudes, but the ice abundance is enhanced by a factor of three at 62°N. This could be solely the result of an actual enhancement, or, what is more likely, also partially due to the ice cloud being at higher altitudes, nearer where the most sensitive region (the center) of the FP1 FOV is located. Fits to a comparable sit-and-stare spectrum at 70°N will be quantified once an aerosol limb scan, also at 70°N and recently available, is analyzed. An enhanced abundance of stratospheric ice at higher altitudes is consistent with the analysis of the 506 cm^{-1} feature of HC_3N ice at 62°N and 70°N undertaken by Anderson et al. (2010). Fig. 21 depicts the latitudinal variation of the normal optical thickness of the stratospheric ice cloud that peaks at 160 cm^{-1}, highlighting the clear increase in ice abundance at 62°N. We have suggested previously that this cloud may be due primarily to condensates of the nitriles HCN and HC_3N (see Fig. 15). This speculation is strengthened by noting that the vapor phases of these nitriles show qualitatively the same relative latitudinal distributions as the ice cloud (Coustenis et al., 2007).

An investigation of Titan's stratospheric haze properties between 20 and 560 cm^{-1}, very similar to ours, was conducted by de Kok et al. (2007). Their primary data sets were CIRS limb scans designed for inferring the temperature structure for the lower stratosphere. Their analysis procedures were somewhat different from those we use. Whereas we analyze continuous intensity profiles across the limb at individual wavenumbers, de Kok et al. used a more conventional approach of analyzing spectral averages at selected tangent heights.

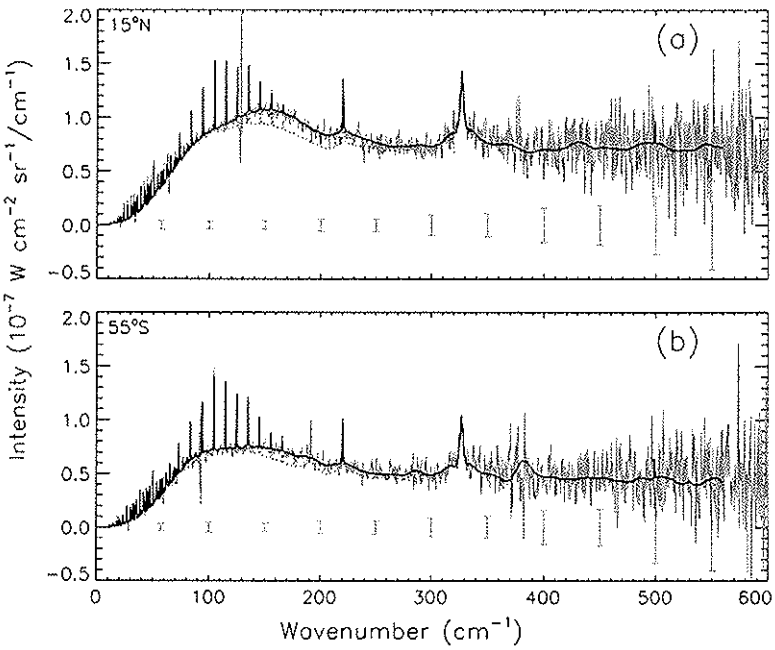

Fig. 19. Observed sit-and-stare spectral averages at (a) 15°N and (b) 55°S are shown in pink at a spectral resolution of 0.5 cm^{-1}. The feature at 380 cm^{-1} (55°S) is due to an 8 Hz noise spike. Relevant characteristics are given in Table 2. Solid black curves are corresponding spectra calculated from the models characterized in Fig. 16a, c and 17a, c. Goodness of comparison is an indicator of degree of internal consistency. Dotted black curves are the solid black curves minus the ice contributions. 1σ uncertainties are indicated by the pink error bars below the data at zero intensity. (For interpretation of the references to colour in this figure legend, the reader is referred to the web version of this article.)

Although the two investigations are similar, there are important differences in perspective and approach, which in turn lead to rather significant differences in the conclusions reached. We examine these differences in some detail.

In order to achieve model solutions that are stable, it is necessary to apply initial constraints to the system. Those that de Kok et al. apply we call phenomenological; they are based on inferences drawn from the shapes of observed features in the spectrum. By contrast our constraints are physical, and involve parameterization of the anticipated distributional characteristics of aerosols and ices (see Section 2).

De Kok et al. identify four components of Titan's haze system: (1) haze 0, of dominant importance between 250 and 560 cm^{-1}, which they associate with the main photochemical aerosol; (2) haze A, a broad feature centered at about 140 cm^{-1} that is separate from the main photochemical aerosol, evident at all latitudes; (3) haze B, another broad feature centered at about 220 cm^{-1}, especially strong at northern high latitudes (see Fig. 20) and non-existent at low and southern latitudes; and (4) haze C, a broad feature centered at 190 cm^{-1}, strongest at some northern high latitudes, but also noticeable at other latitudes.

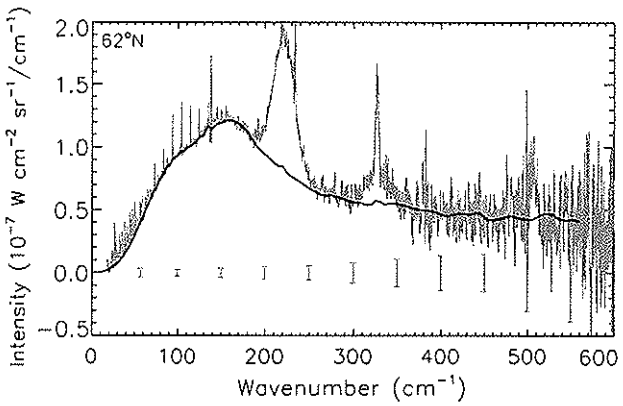

Fig. 20. Observed sit-and-stare average of 24 spectra at a tangent height of 125 km at 62°N is shown in pink. Spectral resolution is 0.5 cm^{-1}. The black curve is an approximate fit to the continuum only, using the same spectral shapes for the aerosol and ice opacities, and the same vertical distributions of abundances, as the 15°S model illustrated in Figs. 10 and 11. Only the magnitude of the ice abundance, and the temperature profile, have been changed. Compared with the 15°S model, the aerosol abundance remains the same and the ice abundance has been increased by a factor of three. The temperature profile for 62°N is adopted from Anderson et al. (2010). 1σ uncertainties are indicated by the pink error bars below the data at zero intensity. No effort to model any of the sharper emission features has been made, since only the continuum is of interest here. (For interpretation of the references to colour in this figure legend, the reader is referred to the web version of this article.)

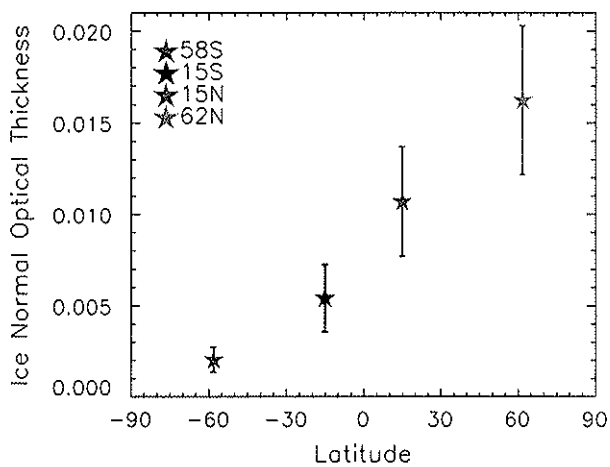

Fig. 21. Latitudinal variation in the normal optical thickness at 160 cm^{-1} of the inferred stratospheric ice cloud that nominally peaks at 90 km. 1σ uncertainties are also shown.

Haze C appears to be very strong at 70°N, but is essentially absent at 85°N. Utilizing this fact, de Kok et al. subtracted the 85°N spectrum directly from the 70°N spectrum at several tangent heights and derived a mean spectral shape for the haze C feature from these observed differences. They state that temperature differences at the two latitudes may affect the relative signals, but do not appear to include this effect in their calculations. Potentially this can lead to systematic errors in their determinations of peak position and spectral shape.

The spectra of hazes A, B, and C overlap to a fair extent. Once their spectral shapes are individually defined, however, these spectral shapes are permanently fixed in the model. This gives rise to two effects: (1) the haze models become sufficiently constrained to yield unique vertical distributions and relative abundances from fits to temperature limb-scan spectra, and (2) because of overlap, any errors in the assumed spectral shape of one feature will translate into incorrect characteristics for an overlapping feature as a result of least-squares fits to the data.

We now compare some of the results of de Kok et al. with ours. Between 250 and 560 cm^{-1}, our aerosol is equivalent to their haze 0. The spectral shapes are very similar, and agree with those derived from Voyager IRIS (Samuelson and Mayo, 1991; Mayo and Samuelson, 2005).

Their haze A is closely associated with our aerosol emission feature at 140 cm^{-1}. However, at southern latitudes de Kok et al. derived a somewhat smaller scale height for haze A than for haze 0, and concluded that the two hazes are different components of Titan's overall haze system. This is contrary to our conclusion that the 140 cm^{-1} emission feature is merely part of an overall single-component aerosol system.

Haze C is most closely related to our stratospheric ice spectrum. Vertical distributions of the two tend to peak at roughly the same altitudes (~90 km), though theirs covers a broader altitude range, extending to higher altitudes. However, their haze C peaks spectrally at 190 cm^{-1}, whereas our ice feature peaks at about 160 cm^{-1}. More importantly, the spectral shape of our ice feature is variable with latitude. This is expected behavior for a composite feature associated with multiple ices, the relative abundances of which vary with latitude. On the other hand, the latitudinal independence of spectral shape for haze C is intrinsic to the model system of de Kok et al., and is a direct consequence of initial constraints imposed on the system.

In general, if one parameter in a given model is in error, a least-squares fit of the model to the data will introduce compensating errors into the other parameters. For example, if the peak position and spectral shape of haze C are somewhat distorted because of the way in which they were derived, this would introduce comparable uncertainties into the overlapping haze A feature. We speculate that this might be one possible source of differences in the scale heights derived for haze 0 and haze A at a common latitude, as well as the reason why these hazes (especially haze A) show increased abundances at southern latitudes near 80 km, where "cross-talk" from an ice cloud layer might be expected. Of course we have no direct proof of these speculations.

Recent studies at shorter wavelengths have been published. An extensive analysis of the latitudinal variation of Titan's haze, using the Cassini Visual and Infrared Mapping Spectrograph (VIMS), spectrally ranging from 0.4 to 1.6 μm, was conducted by Penteado et al. (2010). If methane abundance is assumed constant with latitude, they find the haze density increases by ~60% from 20°S to 10°S, thus defining the boundary of Titan's well-known north/south albedo asymmetry. Results are somewhat uncertain because of an intrinsic ambiguity in separating effects due to haze abundance and methane band strengths. No evidence for stratospheric clouds is presented.

A detailed study of tropospheric clouds, also using VIMS spectra, was undertaken by Brown et al. (2010). Included in the study is evidence for a cloud near the tropopause that appears as a ring around the pole, covering roughly the latitude range 50°N–80°N. No spectral features are identified, but Brown et al. (see also Griffith et al., 2006) suggest a composition of ethane ice, principally because observed vapor abundances indicate that ethane, the most abundant organic besides methane, should condense near the tropopause (see Fig. 1).

Haze properties in the mid infrared (600–1420 cm^{-1}) have been derived from FP3 and FP4 CIRS spectra by Vinatier et al. (2010). The altitude range examined is rather variable with latitude, but tends to be restricted to the stratosphere above 140 km; an exception is at 55°S where the lower limit is about 120 km, still too high to yield information on stratospheric clouds.

Within data uncertainties, the spectral dependence of the haze optical depth is independent of altitude and latitude. This implies a one-component aerosol, consistent with our own conclusions derived from spectra at lower wavenumbers. Analogous to our feature at 140 cm^{-1}, Vinatier et al. find haze spectral emission features centered at 630, 745, and 1390 cm^{-1}.

In all, Vinatier et al. examine nine separate latitudes. Below the 0.4 mbar level (~200 km altitude), all mass mixing ratios increase with altitude. Above this level, those at 40°N, 45°N, and 55°N (at the edge of the polar vortex) decrease with height. There is a general tendency for the ratio of haze-to-gas scale heights to decrease from 1.6–2.4 at 140 km to 0.7–1.2 at about 270 km. Although this is variable with latitude, and observational scatter is large, it is also consistent with our results at lower wavenumbers (see Fig. 16).

Vertical distributions of haze opacities between 0.355 μm and 1.583 μm have been determined from Huygens DISR *in situ* data at 10°S by Tomasko et al. (2008). Results are presented as cumulative aerosol optical depth vs. altitude at 16 separate wavelengths. L. Doose (personal communication) has kindly provided us with volume extinction coefficients vs. altitude at the longest DISR wavelength (1.583 μm). This curve, along with the associated mass extinction coefficient curve, are plotted in Fig. 22. Our results for

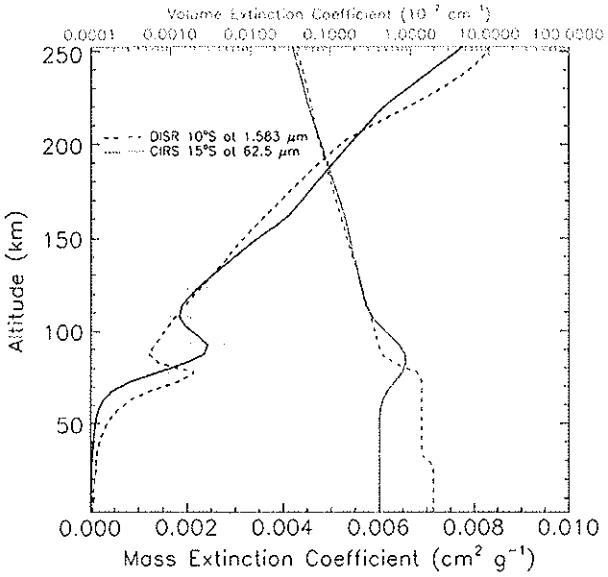

Fig. 22. Comparison of the vertical extinction coefficient profiles of DISR at $\lambda = 1.583$ μm and CIRS at $\lambda = 62.5$ μm ($\nu = 160$ cm^{-1}). Volume and mass extinction profiles are shown in pink and black, respectively. Dashed curves refer to DISR results at 10°S, and solid curves to CIRS results at 15°S. The CIRS absorption coefficients shown in Fig. 10 were multiplied by a factor of 70 for the aerosol and a factor of 20 for the ice before being re-plotted (*i.e.* renormalized) in this figure. 1σ uncertainties are indicated for the CIRS data. (For interpretation of the references to colour in this figure legend, the reader is referred to the web version of this article.)

the nearby latitude 15°S, after being multiplied by the factor 70 for the aerosol and a factor of 20 for the ice, are also replotted here for comparison.

According to Tomasko et al., below 80 km, particle absorption is about half of what it is above 144 km. This is approximately independent of wavelength, although the wavelength dependence of opacity is less jagged below 80 km, suggesting larger particles. Higher single scattering albedos, combined with larger particles, imply condensation of organics may be taking place in the general vicinity of 80 km. Below 30 km the particles appear to grow to a much larger size, suggesting the incorporation of condensed methane into the aerosol.

Agreement between DISR and CIRS FP1 data is far from perfect. Altitudes at which the putative ice cloud layers peak differ by ~15 km, and aerosol extinction coefficient differences in the troposphere lie well outside the formal error bars.

Even so, the comparisons shown in Fig. 22 are highly suggestive, especially after due consideration is given to the following intrinsic dissimilarities. Aerosol volume extinction coefficients depend on particle radius at near-IR wavelengths, although this is not true in the far-IR. On the other hand, ice cloud vertical opacity distributions depend strongly on spectral absorption (emission) features in the far-IR at $\lambda = 62.5$ μm, and therefore on the chemical identity of the ice; at near-IR wavelengths ($\lambda = 1.583$ μm), however, scattering dominates, and the vertical distribution of opacity depends mainly on particle size and overall abundance.

In spite of these dissimilarities, the results for the two spectral regions are roughly comparable after renormalizations of the far-IR opacities by factors of 70 and 20 for the aerosol and the ice, respectively. The factor of 70 is roughly what is expected for an extinction coefficient ratio $N\chi(1.583\ \mu m)/N\chi(62.5\ \mu m)$ for sub-micron aerosol particle sizes relevant to Titan's atmosphere. Renormalization of the ice cloud feature suggests an ice cloud extinction coefficient ratio $N\chi(1.583\ \mu m)/N\chi(62.5\ \mu m) \sim 20$, about three-tenths that for the aerosol. This implies cloud particle radii are no larger than a few microns, consistent with other studies (see Anderson et al. (2010), for a more detailed comparison).

Observational evidence for stratospheric organic ice clouds, even at low latitudes, has thus become quite substantial. Analyses of new CIRS limb-scan and sit-and-stare sequences at 70°N, where stratospheric ices are known to be especially prominent, is in progress, and should increase our understanding of Titan's stratospheric cloud system considerably.

9. Main conclusions

(1) The FIR spectrum of Titan between 20 and 560 cm^{-1} (500–18 μm) indicates the presence of an aerosol that does not change chemical composition noticeably between latitudes of 15°N and 58°S, and between altitudes of 0 and 300 km. This implies that the rate at which aerosol chemistry evolves is much slower than the rate at which dynamical overturning of the atmosphere occurs, at least at these latitudes and altitudes.

(2) The aerosol has a broad emission feature centered approximately at 140 cm^{-1}. We speculate that the feature may be a blended composite that can be identified with low-energy vibrations of two-dimensional lattice structures of large molecules, such as PAHs or nitrogenated aromatics.

(3) There is now strong evidence that stratospheric ice clouds composed of condensed trace organics are global in extent. Although most abundant at high northern latitudes, these clouds extend at least through low latitudes and into southern mid latitudes. They appear to be chemically variable with both latitude and altitude.

(4) There is a broad stratospheric ice cloud feature centered at about 160 cm^{-1} that is roughly compatible with laboratory results for mixtures of HCN and HC_3N ices, though differences do exist. The feature originates from a cloud layer located at an altitude, $z \sim 90$ km, where HCN and HC_3N vapors first saturate and are expected to condense into ices. This altitude also corresponds roughly to the altitude ($z \sim 75$ km) where an increase of opacity in the Huygens DISR near-IR data is evident.

(5) The broad stratospheric ice cloud feature derived near 80 cm^{-1} may be indicative of crystalline C_2H_6, discussed by Schwartz et al. (1971). This potential C_2H_6 ice feature is only evident at latitude 58°S (not at 15°S or 15°N) and is located near an altitude of 60 km, where hydrocarbon vapors (except for methane) are expected to condense into ices.

Acknowledgments

We would like to extend our thanks to Lyn Doose for providing the tabulated Huygens DISR aerosol volume extinction coefficients at 1.583 μm. We also thank Marla Moore for providing laboratory absorption coefficients for HCN and HC_3N ice mixtures. Thanks to Richard Achterberg for providing CIRS Titan temperature structures. C.M.A. was supported in part by the Cassini project and the NASA Cassini Data Analysis Program. R.E.S. was supported in part by the Cassini project and the NSF Planetary Astronomy Program.

References

Achterberg, Richard K., Conrath, Barney J., Gierasch, Peter J., Flasar, Michael F., Nixon, Conor A., 2008. Titan's middle-atmospheric temperatures and dynamics observed by the Cassini Composite Infrared Spectrometer. Icarus 194, 263–277.

Anderson, C.M., Samuelson, R.E., Bjoraker, G.L., Achterberg, R.K., 2010. Particle size and abundance of HC_3N ice in Titan's lower stratosphere at high northern latitudes. Icarus 207, 914–922.

Angus, S., Armstrong, B., de Reuck, K.M., 1976. International thermodynamic tables of the fluid state-5: Methane. In: IUPAC. Pergamon, Oxford.

Armstrong, G.T., Brickwedde, F.G., Scott, R.B., 1955. J. Res. Natl. Bur. Std. 55, 39.

Borysow, A., Frommhold, L., 1986a. Theoretical collision-induced rototranslational absorption spectra for modeling Titan's atmosphere – H_2–N_2 pairs. Astrophys. J. 303, 495–510.

Borysow, A., Frommhold, L., 1986b. Theoretical collision-induced rototranslational absorption spectra for the outer planets – H_2–CH_4 pairs. Astrophys. J. 304, 849–865.

Borysow, A., Frommhold, L., 1986c. Collision induced roto-translational absorption spectra of N_2–N_2 pairs for temperatures from 50 to 300 K. Astrophys. J. 311, 1043–1057.

Borysow, Aleksandra, Frommhold, Lothar, 1987. Collision-induced rototranslational absorption spectra of CH_4–CH_4 pairs at temperatures from 50 to 300 K. Astrophys. J. 318, 940–943.

Borysow, Aleksandra, Tang, Chunmei, 1993. Far infrared CIA spectra of N_2–CH_4 pairs for modeling of Titans atmosphere. Icarus 105, 175–183.

Boudon, V., Pirali, O., Roy, P., Brubach, J.-B., Manceron, L., Vander Auwera, J., in press. The high-resolution far-infrared spectrum of methane at the SOLEIL synchrotron. Icarus.

Brown, Michael E., Roberts, Jessica E., Schaller, Emily L., 2010. Clouds on Titan during the Cassini prime mission: A complete analysis of the VIMS data. Icarus 205, 571–580.

Conrath, B.J., Gierasch, P.J., 1983. Evidence for disequilibrium of ortho and para hydrogen on Jupiter from Voyager IRIS measurements. Nature 306, 571–572.

Courtin, Régis, Wagener, Richard, McKay, Christopher P., Caldwell, John, Fricke, Karl-Heinrich, Raulin, Franco ,is, Bruston, Paul, 1991. UV spectroscopy of Titan's atmosphere, planetary organic chemistry and prebiological synthesis: II. Interpretation of new IUE observations in the 220–335 nm range. Icarus 90, 43–56.

Courtin, R., Gautier, D., McKay, C.P., 1995. Titan's thermal emission spectrum: Reanalysis of the voyager infrared measurements. Icarus 114, 144–162.

Coustenis, A., Lellouch, E., Maillard, J.P., McKay, C.P., 1995. Titan's surface: composition and variability from the near-infrared albedo. Icarus 118, 87–104.

Coustenis, A. et al., 2007. The composition of Titan's stratosphere from Cassini/CIRS mid-infrared spectra. Icarus 189, 35–62.

de Kok, R. et al., 2007. Characteristics of Titan's stratospheric aerosols and condensate clouds from Cassini CIRS far-infrared spectra. Icarus 191, 223–235.

Del Genio, A.D., Zhou, W., Eichler, T.P., 1993. Equatorial superrotation in a slowly rotating GCM: implications for Titan and Venus. Icarus 101, 1–17.

Dello Russo, N., Khanna, R.K., 1996. Laboratory infrared spectroscopic studies of crystalline nitriles with relevance to outer planetary systems. Icarus 123, 366–395.
Dire, James R., 2000. Seasonal photochemical and meridional transport model for the stratosphere of Titan. Icarus 145, 428–444.
Flasar, F.M., Samuelson, R.E., Conrath, B.J., 1981. Titan's atmosphere: Temperature and dynamics. Nature 292, 693–698.
Flasar, F.M. et al., 2004. Exploring the Saturn system in the thermal infrared: The composite infrared spectrometer. Space Sci. Rev. 115, 169–297.
Griffith, C.A. et al., 2006. Evidence for a polar ethane cloud on Titan. Science 313, 1620–1622.
Hanel, R.A., Conrath, B.J., Jennings, D.E., Samuelson, R.E., 2003. Exploration of the Solar System by Infrared Remote Sensing, second ed. Cambridge University Press, UK.
Jacquinet-Husson, N. et al., 2005. The 2003 edition of the GEISA/IASA spectroscopic data base. J. Quant. Spectrosc. Rad. Tran. 95, 429–467.
Jennings, D.E. et al., 2009. Titan's surface brightness temperatures. Astrophys. J. 691, L103–L105.
Karkoschka, Erich, 1994. Spectrophotometry of the jovian planets and Titan at 300- to 1000-nm wavelength: The methane spectrum. Icarus 111, 174–192.
Karkoschka, Erich, 1998. Methane, ammonia, and temperature measurements of the jovian planets and titan from CCD-spectrophotometry. Icarus 1323, 134–146.
Khare, B.N., Sagan, C., Arakawa, E.T., Suits, F., Callcott, T.A., Williams, M.W., 1984. Optical constants of organic tholins produced in a simulated Titanian atmosphere: From soft X-ray to microwave frequencies. Icarus 60, 127–137.
Lacis, A.A., Oinas, V., 1991. A description of the correlated k distribution method for modeling nongray gaseous absorption, thermal emission, and multiple scattering in vertically inhomogeneous atmospheres. J. Geophys. Res. 96, 9027–9063.
Lorenz, R.D., Young, E.F., Lemmon, M.T., 2001. Titan's smile and collar: HST observations of seasonal change 1994–2000. Geophys. Res. Lett. 28, 4453–4456.
Lorenz, Ralph D., Smith, Peter H., Lemmon, Mark T., 2004. Seasonal change in Titan's haze 1992–2002 from Hubble Space Telescope observations. Geophys. Res. Lett. 31, L10702.
Marquardt, D.W., 1963. An algorithm for least-squares estimation of nonlinear parameters. SIAM J. Appl. Math. 11, 431–441.
Mayo, L.M., Samuelson, R.E., 2005. Condensate clouds in Titan's north polar stratosphere. Icarus 176, 316–330.
McKay, C.P., Pollack, J.B., Courtin, R., 1989. The thermal structure of Titan's atmosphere. Icarus 80, 23–53.
McKay, Christopher P., Pollack, James B., Courtin, Regis, 1991. The greenhouse and antigreenhouse effects on Titan. Science 253, 1118–1121.
McKay, C.P., Coustenis, A., Samuelson, R.E., Lemmon, M.T., Lorenz, R.D., Cabane, M., Rannou, P., Drossart, P., 2001. Physical properties of the organic aerosols and clouds on Titan. Planet. Space Sci. 49, 79–99.
Moore, M., Ferrante, Robert F., Moore, James W., Hudson, Reggie, submitted for publication. Infrared spectra and optical constants of nitrile ices relevant to Titans atmosphere. Astrophys. J.
Niemann, H.B. et al., 2005. The abundances of constituents of Titan's atmosphere from the GCMS instrument on the Huygens probe. Nature 438, 779–784.
Penteado, Paulo F. et al., 2010. Latitudinal variations in Titans methane and haze from Cassini VIMS observations. Icarus 206, 352–365.
Rages, K., Pollack, J.B., 1983. Vertical distribution of scattering hazes in Titan's upper atmosphere. Icarus 55, 50–62.
Rages, K., Pollack, J.B., Smith, P.H., 1983. Size estimates of Titan's aerosols based on Voyager high-phase-angle images. J. Geophys. Res. 88, 8721–8728.
Rannou, P., Cabane, M., Chassefiere, E., Botet, R., McKay, C.P., Courtin, R., 1995. Titan's geometric albedo: Role of the fractal structure of the aerosols. Icarus 118, 355–372.
Ricca, Alessandra, Bauschlicher, Charles W., Bakes, E.L.O., 2001. A computational study of the mechanisms for the incorporation of a nitrogen atom into polycyclic aromatic hydrocarbons in the Titan haze. Icarus 154, 516–521.
Rothman, L.S. et al., 2005. The HITRAN 2004 molecular spectroscopic database. J. Quant. Spectrosc. Radiat. Tran. 96, 139–204.
Samuelson, R.E., 1983. Radiative equilibrium model of Titan's atmosphere. Icarus 53, 364–387.
Samuelson, R.E., Mayo, L.A., 1991. Thermal infrared properties of Titan's stratospheric aerosol. Icarus 91, 207–219.
Samuelson, R.E., Hanel, R.A., Kunde, V.G., Maguire, W.C., 1981. Mean molecular weight and hydrogen abundance of Titan's atmosphere. Nature 292, 688–693.
Samuelson, R.E., Nath, N.R., Borysow, A., 1997. Gaseous abundances and methane supersaturation in Titan's troposphere. Planet. Space Sci. 45, 959–980.
Samuelson, R.E., Smith, M.D., Achterberg, R.K., Pearl, J.C., 2007. Cassini CIRS update on stratospheric ices at Titan's winter pole. Icarus 189, 63–71.
Schwartz, Y.A., Ron, A., Kimel, S., 1971. Far-infrared spectral of ethane, ethylene, and acetylene. J. Chem. Phys. 54, 99–105.
Smith, B.A. et al., 1981. Encounter with Saturn – Voyager 1 imaging science results. Science 212, 163–191.
Smith, B.A. et al., 1982. A new look at the Saturn system: The Voyager 2 images. Science 215, 505–537.
Teanby, N.A. et al., 2007. Vertical profiles of HCN, HC_3N, and C_2H_2 in Titan's atmosphere derived from Cassini/CIRS data. Icarus 186, 364–384.
Tomasko, Martin G., West, Robert A., 2009. Aerosols in Titan's atmosphere, in Titan from Cassini-Huygens. Springer.
Tomasko, M.G., Doose, L., Engel, S., Dafoe, L.E., West, R., Lemmon, M., Karkoschka, E., See, C., 2008. A model of Titan's aerosols based on measurements made inside the atmosphere. Planet. Space Sci. 56, 669–707.
Toon, O.B., McKay, C.P., Griffith, C.A., Turco, R.P., 1992. A physical model of Titan's aerosols. Icarus 95, 24–53.
Vinatier, Sandrine et al., 2007. Vertical abundance profiles of hydrocarbons in Titan's atmosphere at 15S and 80N retrieved from Cassini/CIRS spectra. Icarus 188, 120–138.
Vinatier, Sandrine et al., 2010. Analysis of Cassini/CIRS limb spectra of Titan acquired during the nominal mission II. Aerosol extinction profiles in the 600–1420 cm^{-1} spectral range. Icarus 210, 852–866.
Waite, J.H. et al., 2005. Ion neutral mass spectrometer results from the first flyby of Titan. Science 308, 982–986.
Waite, J.H., Young, D.T., Cravens, T.E., Coates, A.J., Crary, F.J., Magee, B., Westlake, J., 2007. The process of tholin formation in Titans upper atmosphere. Science 316, 870–875.
Young, D.T. et al., 2004. Cassini plasma spectrometer investigation. Space Sci. Rev. 114, 1–112.